

1 **Lysosomal degradation ensures accurate chromosomal** 2 **segregation to prevent genomic instability**

3 Eugènia Almacellas^{1,2}, Charles Day^{3,4}, Santiago Ambrosio⁵, Albert Tauler^{1,2*} and Caroline Mauvezin^{2*}

4 Authors information: ¹Department of Biochemistry and Physiology, Faculty of Pharmacy, University of Barcelona,
5 Barcelona 08028, Spain. ²Metabolism and Cancer Laboratory, Molecular Mechanisms and Experimental Therapy in
6 Oncology Program (Oncobell), Bellvitge Biomedical Research Institute IDIBELL, L'Hospitalet del Llobregat 08908,
7 Spain. ³Hormel Institute, University of Minnesota, Austin, Minnesota, 55912, USA. ⁴Neuro-Oncology Program, Mayo
8 Clinic, Rochester, Minnesota, 55905, USA. ⁵Department of Physiological Sciences, Faculty of Medicine and Health
9 Sciences, University of Barcelona, L'Hospitalet del Llobregat 08907, Spain.

10 * Corresponding authors: Dr. Albert Tauler: tauler@ub.edu and Dr. Caroline Mauvezin: cmauvezin@idibell.cat ORCID:
11 0000-0003-4220-7272, Metabolism and Cancer Laboratory, Molecular Mechanisms and Experimental Therapy in
12 Oncology Program (Oncobell), Bellvitge Biomedical Research Institute IDIBELL, L'Hospitalet del Llobregat 08908,
13 Spain.

14 The authors declare no conflict of interest and no competing financial interests.

15 **ABSTRACT**

16 Lysosomes, as primary degradative organelles, are the end-point of different converging
17 pathways including macroautophagy. To date, lysosome function has mainly focused on
18 interphase cells, while their role during mitosis remains controversial. Mitosis dictates the faithful
19 transmission of genetic material among generations, and perturbations of mitotic division lead to
20 chromosomal instability, a hallmark of cancer. Heretofore, correct mitotic progression relies on
21 the orchestrated degradation of mitotic factors, which was mainly attributed to ubiquitin-triggered
22 proteasome-dependent degradation. Here, we show that mitotic transition does not only rely on
23 proteasome-dependent degradation, as impairment of lysosomes increases mitotic timing and
24 leads to mitotic errors, thus promoting chromosomal instability. Furthermore, we identified several
25 putative lysosomal targets in mitotic cells. Among them, WAPL, a cohesin regulatory protein,
26 emerged as a novel p62-interacting protein for targeted lysosomal degradation. Finally,
27 we characterized an atypical nuclear phenotype, the toroidal nucleus, as a novel biomarker for
28 genotoxic screenings. Our results establish lysosome-dependent degradation as an essential
29 event to prevent genomic instability.

30 **KEYWORDS:** Lysosome, Mitosis, Chromosomes segregation, Selective autophagy,
31 Chromosomal instability, Toroidal nucleus.

32 **Abbreviations:** **3D:** three Dimensional; **APC/C:** anaphase-promoting complex; **Arl8b:** ADP-ribosylation
33 factor-like protein 8b; **Atg:** autophagy-related proteins; **BORC:** BLOC-one-related complex; **CDK:** cyclin-
34 dependent kinases; **CENP-E:** centromere-associated protein E; **CIN:** chromosomal instability; **ConcA:**
35 concanamycin A; **CQ:** chloroquine; **DAPI:** 4,6-diamidino-2-penylinole; **FTI:** farnesylation inhibitors; **GFP:**
36 green fluorescent protein; **GO:** gene ontology; **H2B:** histone 2B; **KIF:** kinesin-like protein; **LAMP1/2:**
37 lysosome associated membrane protein 1/2; **LC3:** microtubule-associated protein 1A/1B-light chain 3;
38 **MCAK:** mitotic centromere-associated kinesin; **MEF:** mouse embryonic fibroblast; **NPC:** nuclear pore
39 complex; **PDS5B:** cohesin associated factor B; **SAC:** spindle assembly checkpoint; **SKIP:** pleckstrin
40 homology domain-containing family M member 2; **TEM:** transmission electron microscopy; **ULK1:** unc-51
41 like autophagy activating kinase 1; **UPS:** ubiquitin-proteasome system; **v-ATPase:** vacuolar-ATPases;
42 **WAPL:** wings apart-like protein.

43 INTRODUCTION

44 Chromosomal instability (CIN) is defined as an abnormal loss or rearrangement of chromosomes
45 during cell division¹ and positively correlates with poor cancer patient prognosis². The
46 mechanisms underlying CIN remain poorly characterized but reflect abnormalities in kinetochore-
47 microtubule attachment, sister chromatids cohesion, centrosome duplication, telomeres or the
48 spindle assembly checkpoint (SAC)³.

49 To maintain genome integrity, the cell cycle must be tightly coordinated to ensure the faithful
50 transmission of hereditary information between generations. Cells spend more than 90% of their
51 time in interphase and interphase length correlates with total length of the cell cycle⁴. In contrast,
52 mitosis is extremely short, and the time spent in mitosis is remarkably constant and uncoupled
53 from variability in other phases. Mitosis is the process by which a cell properly divides its genetic
54 material and consists of five active phases from prophase to telophase. The major mitotic
55 checkpoint comprises the metaphase-to-anaphase transition, separating mitotic entry and exit.
56 Coordination of the mitotic regulatory network relies on hierarchal phosphorylation cascades
57 driven by cyclin-dependent kinases (CDK)^{5,6} and the ubiquitin-proteasome system (UPS) under
58 the control of the anaphase-promoting complex (APC/C)^{7,8}. During mitosis, known degradative
59 functions are mainly restricted to UPS, specialized in ubiquitin-triggered protein degradation and
60 presumably faster than lysosome-dependent degradation.

61 Lysosomes are acidic cytosolic vesicles responsible to enzymatically degrade all types of
62 biological material. During macroautophagy, double-membrane vesicles (autophagosomes)
63 engulf cytosolic material, converge and fuse with lysosomes. The lysosomal proton pump v-
64 ATPase drives lumen acidification while the BORC-associated protein complex, including KIF5B
65 motor protein, is the main driver of anterograde lysosomal transport and also contributes to
66 autophagosome-lysosome fusion⁹⁻¹¹. Autophagy-dependent degradation of cargos can either be

67 non-selective (bulk) or targeted (selective). Adaptor proteins, such as p62 (also known as
68 Sequestosome-1) regulate selective autophagic degradation^{12,13}. Being cytosolic vesicles,
69 research on autophagy and lysosomes has mainly focused on interphase cells, omitting their
70 implication on mitosis. As cells undergo mitosis, dramatic structural rearrangements of organelles
71 occur^{14–16}. However, several recent studies show controversial observations about the function of
72 lysosomes and autophagy in mitosis. Some studies claim that autophagy signaling is shut-down
73 at mitotic entry, that autophagic structures are barely detected in dividing cells and that
74 proteasome-dependent degradation of WIPI2 upon mitotic induction suppress autophagic flux^{17–}
75 ¹⁹. In contrast, lysosomal-dependent degradation is implicated in Cyclin A2 proteolysis during
76 mitosis²⁰ and mitophagy is active in prophase^{21,22}. ULK1, an autophagy initiator protein, was
77 shown to drive SAC recruitment to kinetochores through Mad1 phosphorylation²³. Furthermore,
78 selective autophagic degradation of centriolar satellites was recently demonstrated to support
79 correct karyokinesis^{24,25}. Loss of Beclin1, another key autophagic protein, induced gene
80 amplification and consequent aneuploidy²⁶. Better understanding of the regulatory mechanisms
81 driving mitotic transitions is crucial for preventing CIN and developing novel cancer treatment
82 strategies.

83 Here, we show, for the first time, that correct mitotic progression does not rely only on UPS-
84 dependent degradation. Dissecting the mitotic transition, we define a novel function of selective
85 autophagy and lysosome-dependent degradation specifically in dividing cells and identify new
86 mitotic lysosomal substrates. Furthermore, impairment of lysosome function during cell division
87 triggers chromosome mis-segregation and induces a striking nuclear phenotype, the toroidal
88 nucleus, which provides a new tool for genotoxicity tests.

89

90 RESULTS

91 Lysosomes and autophagic vesicles are present and active during cell division

92 To investigate the presence of lysosomes in mitotic subphases, LAMP2-positive vesicles and
93 DAPI-stained DNA were analyzed by immunofluorescence. Here we showed that lysosomes are
94 present and dynamic in all mitotic subphases (**Fig.1A; Video 1**). Morphological analysis of mitotic
95 lysosomes indicated that lysosomes decreased in number while increased in size from prophase
96 to late telophase, when they started recovering their interphase-like morphology (**Fig.1A-C; Video**
97 **1**). In addition, lysosome distribution is modified once cells proceeded into cell division. Mitotic
98 lysosomes surrounded the chromosomes in prophase and moved to the edges of chromosomes
99 during anaphase/telophase until chromosomes decondensed (**Fig.1D**). To analyze whether
100 mitotic lysosomes maintain their degradation capacity during cell division, we stained live U2OS
101 cells stably expressing Histone 2B-GFP (H2B-GFP U2OS) with Lysosensor for acidic organelle
102 detection and MagicRed for lysosomal cathepsin B activation. Colocalization between Lysosensor
103 and MagicRed supported the presence of functional lysosomes in dividing cells (**Fig.1E**).

104 As we found that lysosomes are present and active in mitosis, we analyzed the autophagic flux
105 during cell division. To this end, the expression of p62 and the lipidated form of LC3 (LC3-II) were
106 analyzed in mitosis after inhibition of lysosomal acidification with ConcA. Established
107 synchronization protocols such as serum starvation or double-thymidine block were insufficient to
108 efficiently synchronize U2OS cells in G2. Therefore, based on the ability of CDK1-specific inhibitor
109 RO3306 to reversibly block cells in G2, we established a synchronization-release protocol to
110 obtain enriched mitotic population (**Fig.1F**). Cell cycle analysis validated the efficiency of the
111 protocol in control cells or upon lysosome inhibition (**Fig.1G**). Upon ConcA treatment,
112 synchronized cells showed specific accumulation of LC3-II and of the autophagic adaptor protein
113 p62 without major changes in the global cell cycle profile (**Fig.1G-H**). Time-course assay after cell

114 synchronization and release demonstrated that both autophagic proteins LC3-II and p62 gradually
115 accumulated during mitosis transition upon acidification blockade (**Fig.S1A-B**). In parallel,
116 immunofluorescence analysis of both endogenous LC3 and p62 corroborated the presence of
117 autophagic vesicles in dividing cells (**Fig.1I**). Indeed, Pearson's correlation coefficient (Rr)
118 between LC3 and p62 significantly increased during mitotic subphases compared to interphase
119 cells (**Fig. 1I**). Finally, double-membrane vesicles (autophagosomes), as well as dense single-
120 membrane vesicles (autolysosomes/lysosomes), were detected by Transmission Electron
121 Microscopy (TEM) in mitotic cells (**Fig.1J**).

122 Collectively, our results demonstrate that both autophagic vesicles and functional lysosomes are
123 present and active in mitotic cells.

124 **Lysosome acidification capacity and trafficking maintain correct mitotic progression**

125 To investigate the role of lysosomes in cell division, we studied mitotic cells with impaired
126 lysosomes either by inhibiting their degradative capacity or their intracellular trafficking.
127 Impairment of lysosome acidification by the v-ATPase inhibitor Concanamycin A (ConcA) led to
128 a reduced number of mitotic lysosomes while increasing lysosome size, according to their
129 defective degradation capacity (**Fig.2A, C-D**). Parallel to ConcA treatment, we assessed the effect
130 of KIF5B depletion on lysosome morphology, number and distribution in mitotic cells. While in
131 interphase, KIF5B depletion induced a dramatic clustering of lysosomes in the perinuclear region
132 and a reduction in the lysosomal number. However, these effects were negligible in mitotic cells.
133 Interestingly, KIF5B depletion did not affect either lysosome number or size in dividing cells
134 (**Fig.2B-E and Fig.S2A**). When we analyzed the lysosomal distribution in the different mitotic
135 subphases, we observed that the hierarchical distribution of lysosomes observed in control cells
136 was almost completely absent in KIF5B-depleted cells (**Fig.2E**). Interestingly, in this setting,
137 KIF5B did not induce a clustering of lysosomes in a central zone as in interphase but impeded

138 the spatial organization of lysosomes during mitosis suggesting the implication of this kinesin on
139 the heterogeneous distribution of lysosomes during mitosis (**Fig.2E**).

140 Mitotic timing is strictly regulated and remarkably constant among different cell types and
141 species⁴, taking approximately one hour in normal mitosis. Thus, after identifying active
142 lysosomes in mitotic cells the direct implication of lysosomes in mitotic progression was tested.
143 To this end, we used live-imaging to analyze H2B-GFP U2OS cells treated with ConcA or KIF5B-
144 depleted and recorded mitotic timing from prophase (chromosome condensation) to telophase
145 (chromosome decondensation). Mitosis was 22% slower in ConcA-treated cells compared to
146 control, and KIF5B depletion delayed mitotic progression to the same extent (**Fig.2F-G; Videos**
147 **2-4**). Combination of ConcA-treatment with KIF5B knockdown increased the average mitotic
148 duration by 45% verse control (**Fig.2G**).

149 In all, integrity of both lysosome transport and functionality is key for preserving mitotic schedule.
150 To precisely characterize the involvement of lysosomes in mitotic progression, we separately
151 analyzed the timing of mitotic entry (prophase to metaphase) and exit (metaphase to telophase).
152 Interestingly, both episodes were delayed by treatments that impaired lysosomes (**Fig.S2B**).
153 Consistently, the additive effect was reflected in both mitotic entry and exit (**Fig.S2B**).

154 One of the main causes of mitotic delay is the accumulation of mitotic errors such as misaligned
155 chromosomes at metaphase plate or chromosome bridges appearing during chromosome
156 segregation in anaphase²⁷ (**Fig.2H**). Thus, we next quantified the acquirement of mitotic errors in
157 synchronized cells treated or not with ConcA. Our results demonstrated that lysosome
158 acidification blockade significantly induces the accumulation of misaligned chromosomes and
159 chromosome bridges (**Fig.2I**). In parallel, we tested whether, beyond acidification, the protective
160 role of lysosomes against mitotic errors also relies on trafficking. Consistent with the observed
161 mitotic delay (**Fig.2F-G**), KIF5B-depleted synchronized cells showed a higher frequency of both

162 types of mitotic errors (**Fig.2J**). Thus, active lysosomes are important organelles to ensure correct
163 mitosis progression and limit CIN signature.

164 **Mitotic errors induced by lysosome impairment correlate with an abnormal nuclear**
165 **phenotype: the toroidal nucleus**

166 Defective mitotic progression generated a robust and striking nuclear phenotype in interphase
167 cells. Precisely, we observed a DAPI-stained nucleus with a hole devoid of chromatin (**Fig.3A**).
168 To understand how this structure was originated, we followed the change on nuclear structure
169 during mitosis by live-imaging using H2B-GFP U2OS cells. Our results showed that this
170 unconventional nuclear phenotype forms upon mitosis, being detectable in at least one of the
171 daughter cells once chromosomes decondense (**Fig.3B; Video 5**). To assure that this
172 unconventional structure does not correspond to an enlarged nucleolus²⁸, immunofluorescence
173 analysis was performed and results showed that none of the tested nucleolar markers (nucleolin,
174 fibrillarin and UBF) co-stained with the DAPI-free area (**Fig.3C and S3A**). To resolve whether this
175 section is nuclear or cytosolic, we imaged the nuclear envelope by immunofluorescence using
176 Lamin B1 and Nuclear Pore Complex (NPC) antibodies (**Fig.3D and S3B**). Interestingly, the
177 nuclear envelope was correctly formed around DNA. Further immunofluorescence analysis
178 showed that cytoskeleton filaments such as Phalloidin-stained actin fibers and microtubules, as
179 well as LAMP2-positive lysosomes or LC3-p62-positive autophagosomes were present within e
180 void at the center of the nuclei (**Fig.3E and S3C-D**). To discard a nuclear invagination and/or an
181 artifact, 3D reconstruction of high-quality images using IMARIS software resulted in the
182 characterization of a donut-like shaped structure that we refer to as a “toroidal nucleus” (**Fig.3F**
183 and **Video 6**). Ultrastructure analysis of these toroidal nuclei by TEM confirmed that cytosolic
184 material, including autophagic vesicles and lysosomes were present within the hole (**Fig.3G**).

185 This phenotype was once reported as donut-shaped nucleus²⁹. The authors proposed that protein
186 farnesylation inhibitors (FTI) induce the formation of toroidal nuclei by causing a pericentrin-
187 related centrosome separation defect in HeLa cells. Thus, we tested whether FTI induced the
188 formation of toroidal nuclei in our model. After confirming the production of toroidal nuclei following
189 FTI treatment in HeLa cells (**Fig.S3E, left**), we demonstrated that U2OS cells did not respond to
190 FTI. This is contrast to our results with impairment of lysosome acidification by ConcA, which
191 significantly increased the percentage of toroidal nuclei in both cell types (**Fig.S3E, right**). To
192 verify that FTI does not stimulate toroidal nuclei formation with a different kinetics in U2OS, we
193 treated and analyzed cells for 24h, 48h and 72h with FTI or ConcA. While ConcA gradually
194 induced a robust increase of toroidal nuclei with time; FTI did not (**Fig.S3F**). Next, we analyzed
195 whether inhibition of lysosome acidification by ConcA or Chloroquine (CQ) induced the inhibition
196 of farnesylation of Lamin A/C. Neither ConcA nor CQ do not impede Lamin A/C farnesylation like
197 FTI (**Fig.S3G**). Our results suggest that the formation of toroidal nuclei is not due to the inhibition
198 of farnesylation *per se* but to a defect in mitotic progression regardless its inducer.

199 Mitotic stresses have been linked to prolonged mitosis and accumulation of mitotic errors, both of
200 which we detected after lysosomal impairment. As toroidal nuclei were formed following
201 karyokinesis, we examined by live imaging a putative link between the occurrence of mitotic errors
202 and the formation of toroidal nuclei. The results showed a linear correlation between detectable
203 mitotic errors and toroidal nucleus generation with a Pearson's correlation coefficient of 0.85
204 (**Fig.3H**). Indeed, single-cell analysis demonstrated that more than 80% of toroidal nuclei resulted
205 from cells undergoing apparent defective mitosis (**Fig.3I**). Based on this, we next investigated the
206 role of mitotic stresses on generating toroidal nuclei. To this end, we depleted cells of KIF11, a
207 kinesin required for bipolar spindle establishment³⁰, and analyzed the formation of toroidal nuclei.
208 Disruption of KIF11 by small interfering RNA (siKIF11) or by the KIF11 specific inhibitor Monastrol
209 induced a significant increase in toroidal nucleus frequency (**Fig.3J**) without dramatically affecting

210 lysosome morphology and localization (**Fig.S3H**). Depletion of other kinesins implicated in
211 chromosome segregation such as mitotic centromere-associated kinesin (siMCAK/KIF2C)³¹ or
212 Centromere-associated protein E (siCENP-E)³² produced a 3.3- and 3.8-fold increase of toroidal
213 nucleus population, respectively (**Fig.S3I**). In all tested conditions, lysosomes morphology or
214 distribution were not apparently perturbed (**Fig.S3J**). Furthermore, cells treated with Nocodazole,
215 a microtubule de-polymerizing agent, showed a 4.5-fold increased prevalence of toroidal nuclei
216 accompanied by the expected lysosomal collapse (**Fig.S3I-J**). Thus, the formation of toroidal
217 nucleus seems to be attributable to impairment of karyokinesis.

218 We next investigated whether this phenotype is a consequence of impaired nuclear envelope
219 reformation. Live imaging of H2B-GFP U2OS cells stably expressing mCherry-Lamin A/C,
220 indicated that the reformation of the nuclear envelope preceded the formation of toroidal nuclei
221 (**Fig.S3K; Video 7**). This nuclear phenotype was versatile in terms of size, nuclear localization
222 and morphology (**Fig.S3L1-4**). Furthermore, the nucleus could contain more than one void
223 (**Fig.S3L5-8**) and be accompanied by micronucleus (**Fig.S3L6**). After mitosis, one or both
224 daughter cells could harbor this phenotype (**Fig.S3L7-8**).

225 We investigated whether toroidal nucleus was a common feature or specific to U2OS cells. To
226 this end, we screened through a panel of cell lines. Toroidal nuclei were not detected under the
227 tested conditions in the colon carcinoma cell lines RKO, LoVo or HCT116, hepatocarcinoma cells
228 Huh7 or MC-PED17 glioma-derived cell line³³⁻³⁶ (**Fig.3K**). However, detection of toroidal nuclei
229 was successful in various cells, among which non-transformed human skin fibroblast (HFF) and
230 embryonic mouse fibroblasts (MEF), as well as cells from lung carcinoma (A549), cervix
231 carcinoma (HeLa) or diffuse intrinsic pontine glioma (SU-DIPG-XVII, SF-8628 and SF-7761)^{33,34,37}
232 (**Fig.3K-L**). All those cells, except SF-8628, responded to Conca treatment by presenting a
233 significant increase of toroidal nuclei (**Fig.3K**).

234 Thus, toroidal nuclei can be scored as a read-out for mitotic errors in interphase cells.

235 **Lysosome disruption induces the formation of toroidal nuclei**

236 The presence of toroidal nuclei in interphase cells facilitates the analysis of mitotic impairment in
237 whole cell populations, favoring the toroidal nucleus as a powerful tool for quantitative analysis of
238 chromosomal instability. Here we aimed to screen for lysosome-specific stresses using toroidal
239 nucleus as a biomarker for chromosomal instability. To this end, cells were treated with ConcA or
240 depleted for KIF5B and toroidal nuclei frequency was quantified. Consistently, v-ATPase inhibition
241 as well as blockage of anterograde transport led to a robust increase of toroidal nuclei population
242 **(Fig.4A-B)**.

243 To discard ConcA-side effects not related to v-ATPase inhibition, we genetically or chemically
244 inhibited lysosome acidification. Thus, cells were treated with Chloroquine or depleted of the V0c
245 v-ATPase subunit (siATP6V0c). In agreement, inhibition of lysosome acidification increased the
246 formation of toroidal nucleus by 2.5-3-fold **(Fig.4C)**. To validate treatment efficiency, lysosome
247 positioning and size were assessed by immunofluorescence, confirming the expected increase in
248 lysosomal volume³⁸ **(Fig.4D)**. Both ConcA and Chloroquine increased toroidal nucleus formation
249 but their kinetics differed **(Fig.S4A)**. Indeed, ConcA treatment acted faster and produced a peak
250 effect at 24 hours, while Chloroquine produced a similar effect after 48 hours, inducing the
251 maximum impact at 72 hours **(Fig.S4A)**. To corroborate the specificity of mitosis impairment to
252 lysosome-related stresses, we tested compounds targeting other cellular processes or
253 organelles. In contrast to lysosomal inhibition, treatment with the mitochondrial complex I inhibitor
254 Phenformin or the proteasome inhibitor MG132 had no significant effect on the frequency of
255 toroidal nuclei in unsynchronized cells **(Fig.S4B)**. We further asked whether defects in BORC-
256 dependent lysosome trafficking would also induce formation of toroidal nuclei as we determined
257 in cells depleted for KIF5B **(Fig.4E)**. Cells genetically depleted of BORC-associated proteins Arl8b

258 or SKIP also showed a significant increase in the population of toroidal nuclei (2.3- and 4.1-fold
259 respectively) confirming the importance of lysosomal trafficking for correct mitotic progression
260 (**Fig.4F**). Depletion efficacy was corroborated by the perinuclear clustering of lysosomes (**Fig.4F**).
261 Additionally, we examined the specificity of the motor function of KIF5B in the formation of toroidal
262 nucleus by complementing control or KIF5B-depleted cells with neuronal KIF5A, which resulted
263 in a rescue of normal toroidal nucleus frequency (**Fig.4G**). Interestingly, depletion of other motor
264 proteins involved in lysosomal trafficking such as KIF3A, KIF2A or KIF1A also led to a significant
265 increase in toroidal nuclei (**Fig.S4C**). Parallel to a delay in mitotic timing (**Fig.2F-G**), we found that
266 simultaneous disruption of lysosome acidification (ConcA) and trafficking (siKIF5B or siSKIP) had
267 an additive effect on toroidal nucleus formation compared to single treatments (**Fig.4H**). In all, our
268 results confirm that both v-ATPase-dependent lysosome acidification and BORC-associated
269 lysosomal trafficking are required to preserve mitotic integrity.

270 Impairment of lysosome functionality does not prevent mitotic cells to progress into G1 phase but
271 leads to CIN. In cells synchronized and released specifically in mitosis, ConcA and Chloroquine
272 similarly led to toroidal nuclei formation (2.6- and 2.7-fold increase, respectively) (**Fig.S4D**),
273 indicating that the different kinetics observed might be due to effect of the drugs in other phases
274 of the cell cycle. Interestingly, neither MG132 nor Monastrol induced toroidal nuclei in these
275 conditions (**Fig.S4D**), but it is noteworthy that these drugs impeded cells from properly concluding
276 cell division as previously demonstrated^{39,40}, thus limiting the generation of subsequent daughter
277 cells harboring toroidal nucleus (**Fig.S4E**). These results further suggest that lysosomes are not
278 required to undergo mitosis, but genomic instability is triggered when lysosomes are impaired.

279 **Macroautophagy is a key player to maintain mitosis fidelity**

280 As we have detected the presence of autophagic vesicles in mitosis (**Fig.1**), we next analyzed
281 the involvement of macroautophagy for faithful mitotic progression by scoring for toroidal nucleus

282 frequency after macroautophagy inhibition. Genetic depletion of Atg5 (siAtg5) induced a
283 significant increase in the proportion of toroidal nuclei (1.6-fold increase) (**Fig.5A**). Notably,
284 ConcA did not significantly affect the formation of toroidal nucleus in Atg5-depleted cells (**Fig.5A**).
285 In agreement with the correlation between mitotic errors occurrence and formation of toroidal
286 nuclei, the inhibition of autophagy by Atg5 depletion provoked a significant increase in misaligned
287 chromosomes and chromosome bridges (**Fig.5B-C**). Protein depletion efficiency was monitored
288 by Western Blot (**Fig.S5A**). Chemical inhibition of autophagy by 3MA, a PI3K-class III inhibitor,
289 also resulted in an increase in toroidal nuclei frequency together with an enhanced detection of
290 chromosomal misalignment (**Fig.S5B-C**). As U2OS is a cancer cell line already susceptible to
291 genomic instability and chromosome alterations⁴¹, we used mouse embryonic fibroblasts (MEFs)
292 to analyze the impact of defective autophagy on mitotic progression in a non-tumoral model. First,
293 we validated ConcA efficiency and autophagic flux impairment by analyzing Atg5 and LC3 protein
294 levels. As expected, Atg5^{-/-} MEFs harbored a defective autophagic flux (**Fig.5D**). Then, we
295 quantified the frequency of toroidal nuclei in Atg5 wt (Atg5^{+/+}) and Atg5 KO (Atg5^{-/-}) MEFs.
296 ConcA treatment in Atg5^{+/+} MEFs significantly increased toroidal nuclei population,
297 demonstrating that lysosomal inhibition impacts mitotic progression in various cell lines (**Fig.5E-**
298 **F and Fig.3K-L**). Like the effect of the depletion of Atg5 in U2OS cells, Atg5^{-/-} MEFs presented
299 a significantly increased percentage of toroidal nuclei under normal growing conditions,
300 supporting that basal autophagy prevents cells from mitotic errors. ConcA-induced toroidal
301 nucleus formation was not further increased in Atg5 KO MEFs (**Fig.5E**). Atg5-deficient MEFs were
302 significantly more susceptible to chromosomal misalignment and chromosomal bridges compared
303 to parental MEFs (2.36- and 1.48-fold increase respectively) (**Fig.5G-H**). Inhibition of v-ATPase-
304 dependent lysosomal acidification by ConcA clearly increased chromosome misalignment and
305 chromosomal bridges in control Atg5^{+/+} MEFs (**Fig.5G-H**). Cells lacking Atg5 showed a milder
306 response to inhibition of lysosomal acidification regarding both phenotypes (**Fig.5G-H**).

307 Altogether, our results establish the involvement of macroautophagy machinery in correct mitotic
308 progression.

309 **Cohesin proteins WAPL and PDS5B are novel lysosome substrates during cell division**

310 Based on the characterization of a remarkable role for lysosomes and autophagic vesicles in
311 mitotic progression, we next aimed to identify novel substrates of the autophagic-lysosomal
312 pathway specifically in mitosis by mass spectrometry analysis. Following synchronization of cells
313 at G2/M transition, cells were released in normal media or in media containing ConcA for 7 hours.
314 G1-enriched cell fractions were processed for mass spectrometry analysis. Drug efficacy was
315 validated by LC3 and p62 accumulation in the three experimental replicates after ConcA treatment
316 (**Fig.S6A**). Proteomic data analysis identified a total of 1749 peptides present in both ConcA and
317 control fractions, while only 13 and 141 were uniquely detected in control and ConcA fractions,
318 respectively (**Fig.6A**). Enrichment analysis validated 853 peptides being differently expressed (q -
319 value <0.05) that were selected based on ± 1.2 -fold change cut-off (**Fig.6B**). In concordance with
320 its role in inhibiting lysosome-dependent degradation, ConcA significantly induces protein
321 accumulation. The obtained list of candidates was clustered into cellular and organism functions
322 using Reactome free database^{42,43}. Reactome analysis highlighted that proteins accumulated
323 after lysosome inhibition specifically during mitosis were mainly involved in cell cycle, vesicle-
324 mediated transport or DNA repair (**Fig.S6B**). In agreement with previous data (**Fig.1I, S1B** and
325 **S6A**), p62 was significantly increased by 2.73-fold in the ConcA fraction compared to control
326 (**Fig.6B**). Next, we selected the 56 protein candidates that were clustered in functional
327 annotations related to mitosis and cell cycle regulation and we performed a GO enrichment
328 analysis (**Fig.S6C**). A list of 20 proteins involved in mitotic cell cycle progress (GO:1903047) were
329 further studied to define the involvement of lysosomes in chromosome segregation (**Fig.6C**).
330 Interestingly, among the principal enriched proteins, two cofactors of the cohesin complex such

331 as Cohesin-associated factor B (PDS5B) and Wings apart-like protein (WAPL) were significantly
332 increased by 4.78- and 1.64-fold, respectively (**Fig.6B-C**). To validate proteomic data, we isolated
333 mitotic cells by shake-off after synchronization-release and evaluated protein levels in control and
334 ConcA-treated cells. As expected, autophagic proteins p62 and LC3-II accumulated in ConcA-
335 treated mitotic fraction (**Fig.6D and S6D**). Significant increase of both WAPL and PDS5B protein
336 levels occurred in mitotic cells upon acute impairment of lysosomal acidification capacity (**Fig.6D-**
337 **E**), indicating that both PDS5B and WAPL are novel putative lysosomal substrates specifically
338 during mitotic progression. To validate our findings in another cell line, we obtained shake-off
339 fractions from non-transformed MEFs. Mitotic fractions of non-synchronized MEFs corroborated
340 that PDS5B and WAPL significantly accumulated more in Atg5 ^{-/-} MEFs cells compared to
341 parental MEFs (**Fig.6F-G and S6E**). WAPL and PDS5B accumulation upon lysosome inhibition
342 could potentially be due to the observed mitotic delay independent of the autophagy machinery.
343 To address this point, U2OS cells were transfected with exogenous WAPL-GFP protein and
344 treated or not with ConcA for 3 hours after synchronization. Mitosis-enriched fractions were then
345 subjected to GFP-immunoprecipitation. First, we validated the binding between WAPL and its
346 well-described partner PDS5B⁴⁴ (**Fig.6H**). WAPL-GFP interacts with PDS5B to the same extent
347 in control or ConcA-treated cells, suggesting that their interaction is maintained upon lysosomal
348 inhibition. Interestingly, WAPL-GFP interaction with autophagic adaptor protein p62 significantly
349 increased in ConcA-treated cells (**Fig.6H**). These results support that WAPL is recognized by
350 p62-dependent selective autophagy machinery and emerges as a novel lysosome substrate
351 during mitosis.

352 In all, our results shed light into a novel regulatory mechanism for accurate mitotic progression,
353 depicting lysosomes as key players for correct chromosomal congression and faithful genetic
354 transmission (**Fig.7**). In addition, we identified the toroidal nuclei as a read-out of mitotic defects
355 in interphase cells, and such, are a novel biomarker of genotoxicity for cancer research.

356 **DISCUSSION**

357 **Faithful mitotic progression relies on autophagy and lysosomes**

358 During mitosis, dramatic cellular rearrangement occurs to support proper chromosome
359 segregation and productive partitioning of intracellular organelles. Many membranous
360 compartments undergo massive spatiotemporal disruption¹⁶ and scheduled protein degradation
361 is required. While the role of UPS has been extensively studied, the implication of lysosomes and
362 autophagy in cell division still remains elusive^{17,18,20–23,45}. Although lysosome studies are mainly
363 focused on interphase cells, endocytic vesicles (including lysosomes) were proposed to serve as
364 a membrane source for plasma membrane extension and retraction during mitotic transition^{14,15}.
365 Recently, PCM1-driven selective degradation of centriolar satellites was shown to maintain
366 centrosome function for correct mitotic progression²⁴. Here, our results agree with the persistence
367 of a robust autophagic flux and lysosomal-dependent degradation during mitosis. Lysosome
368 enlargement suggests that fusion events are occurring in early mitosis and that, in contrast to
369 other organelles, lysosomes play an active role during cell division. The finding that under basal
370 conditions Atg5 KO MEFs harbor a higher population of toroidal nuclei corroborates that
371 autophagy is active and necessary for mitosis even in non-transformed cells. Among the identified
372 lysosomal substrates in mitosis, the accumulation of p62, an autophagic adaptor protein for
373 ubiquitinated cargos, validates the persistence of autophagic flux and suggests a potential
374 alternative route for the degradation of mitotic factors^{46,47}. To note, PCM1 was not detected in our
375 proteomic analysis of mitotic cells, supporting that various selective autophagy processes might
376 probably coexist and should be timely regulated during mitotic progression. Recently, p62
377 emerged as a potential pivotal player in the crosstalk between UPS and selective
378 autophagosome-lysosome degradation^{48,49}. Based on p62 bifunctionality and ubiquitin-lysine
379 linkages diversity, we speculate a potential interconnection between the two main degradative

380 pathways to correctly distribute genetic material. Control of sister chromatid cohesion during cell
381 division is crucial for equal distribution of genetic material. The canonical evolutionary conserved
382 cohesin complex is one of the main molecular entities involved in this process. The cohesin
383 complex consists of four subunits (SMC1, SMC3, SCC1 and STAG1/3)⁵⁰. Currently, most
384 research focuses on cohesin loading processes during replication and cohesin-dependent
385 extrusion of chromatin loops for DNA-damage repair⁵¹. In mitosis, cohesin supports both mitotic
386 entry and metaphase-to-anaphase transition. In prophase, cohesin complexes dissociate to allow
387 chromatid condensation and separation. At that precise moment, cohesin complex disruption is
388 triggered by WAPL and PDS5B along the chromatids arms^{52,53}. WAPL-dependent dissociation at
389 the centromeric region is inhibited by Shugoshin to prevent premature chromatin separation^{54,55}.
390 During metaphase-to-anaphase transition, chromosome dissociation at the centromeric region is
391 regulated by APC/C-dependent securin ubiquitination, leading to separase activation that cleaves
392 SCC1 to culminate chromatids separation⁵⁶. Since lysosomes can degrade most biological
393 material and, taking in account that in this study we identified more than 100 potential lysosomal
394 protein substrates in mitotic cells, we favor the idea that the implication of lysosomes in cell
395 division is a multifactorial process. Our finding that WAPL and PDS5B accumulate upon blockade
396 of lysosomal acidification, identifies them as potential lysosomal substrates specifically during
397 mitosis. Our study reports for the first time the involvement of autophagy- and lysosomal-
398 dependent degradation of cohesin cofactors. The identification of WAPL as a novel p62 interactor
399 supports the model of selective degradation of WAPL by lysosome during mitotic transition.
400 However, additional studies would be needed to better understand the interconnection between
401 lysosome-dependent degradation and the regulation of chromatid cohesion during mitotic
402 progression. Variations in PDS5B and WAPL expression correlate cohesin and chromosomal
403 segregation defects with aneuploidies and cancer progression^{52,57-60}.

404 While the implications of lysosome biology in cancer are still controversial, efficacy of
405 lysosomotropic agents has been proven in several malignancies either alone or in combination,
406 and clinical trials are ongoing^{61,62}. CIN is considered a hallmark of cancer understood either as a
407 strength, due to mutation induction facilitating tumor diversification, or as a tumor vulnerability by
408 eventually triggering apoptotic cell death^{2,63}. Defective autophagy was recently linked to increased
409 CIN⁶⁴. Here we show that lysosomal acidification and trafficking as well as selective autophagy
410 are necessary to prevent CIN. Our data are consistent with the metaphor of autophagy and
411 lysosome-dependent degradation as a double-edged sword in cancer progression⁶⁵. In all,
412 depending on cell type and tumor stage, a combination of lysosomotropic drugs with conventional
413 therapies might be beneficial, as autophagy inhibition can be detrimental for cancer cells and
414 increased CIN can lead to cell death. Therefore, better understanding of the mechanisms by which
415 selective autophagy functions in cell division will provide novel routes to improve cancer treatment
416 strategies.

417 **Toroidal nucleus, a new tool for genotoxicity screenings**

418 Study of mitosis is challenging due to the velocity and architectural changes accompanying cell
419 division. To escape these obstacles, most mitosis-focused studies take advantage of
420 synchronization protocols. However, drugs used for cell synchronization, such as Nocodazole, do
421 not specifically target mitosis but rather essential cellular components like microtubules, thus
422 altering basic cellular functions. Currently, the only marker of defective mitosis detectable in non-
423 mitotic cells is the micronucleus. Although micronuclei formation is a consequence of
424 chromosome missegregation⁶⁶, they can be reabsorbed during subsequent cell divisions or
425 destroyed by autophagy^{67,68}. Therefore, complementary read-outs in interphase cells are needed
426 for the analysis of mitosis impairment. Here we show that toroidal nuclei form upon inexact mitosis
427 and linearly correlates with the occurrence of mitotic errors. Inhibition of farnesylation was

428 previously proposed to drive the formation of donut-shaped nuclei by affecting centrosome
429 function²⁹. Here we demonstrate that toroidal nuclei do not specifically and uniquely form upon
430 inhibition of protein farnesylation. Indeed, FTI did not increase toroidal nucleus population in
431 U2OS, while mitotic stresses, such as inhibition of lysosomal function described here, significantly
432 and robustly increased the frequency of toroidal nuclei in various cell lines. In addition, our results
433 reveal that toroidal nuclei form prior to reformation of the nuclear envelope, as it was also
434 described for micronucleus⁶⁹. The fate of micronuclei is still uncertain. Four possibilities are under
435 examination: degradation, reincorporation into the nucleus, extrusion or persistence in the
436 cytoplasm leading to apoptosis or chromothripsis⁷⁰. We expect similarities for toroidal nuclei, but
437 further analyses are needed to decipher how cells can cope with toroidal nuclei. We detected
438 toroidal nuclei in transformed and non-transformed cells, designating presence of this structure
439 as a robust and conserved phenotype within cell lines. However, the occurrence of toroidal nuclei
440 might vary dependent on cell type specificities and/or genetic background. Variability in toroidal
441 nucleus frequency might also correlate with basal autophagy levels, which are known to be cell
442 type specific⁷¹. Noteworthy, detection of toroidal nuclei is a new convenient tool for impaired
443 mitosis in genotoxicity screenings.

444 Until now, orchestration of mitotic factors degradation has been exclusively attributed to the UPS.
445 Our data reveals an additional route in which active autophagy and lysosomes promote faithful
446 genetic transmission. Given the promising results of lysosomotropic drugs for cancer treatment,
447 our study opens an alternative line of research focusing on lysosomes modulation to exploit CIN
448 for cancer therapy.

449 **MATERIALS AND METHODS**

450 **Cell Culture**

451 U2OS, HeLa, A549, HCT116, RKO, Huh7, MCF7 and HEK293-T cell lines were obtained from
452 American Type Culture Collection (ATCC). Atg5 wt and Atg5 KO MEF were kindly provided by
453 Dr. Zorzano (IRB Barcelona). HFF cells were kindly provided by the ICO CellBank. U2OS H2B-
454 GFP cell line was kindly provided by Dr. Agell (UB). SF-7761 and SF-8628 were purchased from
455 Millipore Sigma (Burlington, MA). MC-PED17 cells were a gift from Dave Daniels (Mayo Clinic;
456 Rochester, MN). SU-DIPG-XVII cells were a gift from Michelle Monje (Stanford University; Palo
457 Alto, CA). U2OS mCherry-LaminA/C and U2OS H2B-GFP LAMP1-RFP were generated in our
458 laboratory by transient transfection of plasmids purchased in Addgene repository, LAMP1-GFP
459 (#34831), LAMP1-mRFP-Flag (#34611) and mCherry-LaminA/C (#55068). WAPL-GFP plasmid
460 was kindly shared by Dr. Fangwei Wang. Briefly, DNA transfection was performed following
461 manufacturer's instructions using Lipofectamine 2000 (Life Technologies) in 1:5 opti-MEM:
462 DMEM medium. Cells were selected using a fluorescence-activated cell sorter (MoFlo Atrios
463 SORTER). Cells were grown in DMEM high glucose (Gibco) [4mM L-Glutamine, 4.5 g/L glucose,
464 1 mM Pyruvate] supplemented with 10% heat-inactivated fetal bovine serum (FBS) (Sigma
465 Aldrich). Cells were incubated at 37°C, 5% CO₂ and 90-95% of relative humidity. Specific
466 experimental conditions are indicated in figure legends. All chemicals used in this study are
467 reported in **Table 1**.

468 **Cell synchronization at G2**

469 Cells were seeded the day before starting the synchronization in DMEM medium supplemented
470 with FBS (complete DMEM). Thymidine was added at a final concentration of 2 μM for 24 hours
471 to synchronize cells at late G1. After PBS washing, cells were released to S phase by adding

472 complete DMEM for 2 hours. Finally, RO3306 (CDK1 inhibitor) was added to cell culture medium
473 at a final concentration of 9 μ M for 12 hours to arrest cells at late G2 (**Fig.1F**). Experiments with
474 synchronized cells were performed by releasing cells in complete DMEM with or without the
475 corresponding drugs for the indicated times. For the obtention of shake-off fractions, synchronized
476 cells were subjected to consecutive strokes to the dishes to detach specifically the mitotic cells
477 while maintaining the integrity of the cell monolayer.

478 **Silencing RNA transfections**

479 siRNA transfections were performed following manufacturer's instructions in Opti-MEM medium
480 (Life Technologies) using Lipofectamine RNA-iMAX (Life Technologies). Unless otherwise
481 indicated, transfections were performed for 48 hours. siRNA sequences and concentrations used
482 in these studies are listed in **Table 2**.

483 **Cell Cycle analysis**

484 Cells were trypsinized, counted and placed on ice. 500,000 cells were centrifuged at 1200 rpm at
485 4°C for 5 minutes and cell pellet was washed with ice-cold PBS, fixed with 70% ethanol and
486 placed at -20°C for at least 24 hours. Cells were then washed with ice-cold FACS buffer [BSA
487 0.1%, EDTA 5 mM in PBS] and centrifuged for 5 minutes at 1000 rpm at 4°C. Supernatant was
488 discarded and the cell pellet was resuspended in propidium iodide (PI) staining solution [PBS,
489 0.1% NP40, 20 μ g/mL RNase A (Invitrogen), 40 μ g/mL PI (Sigma)]. Cell suspension was
490 transferred to a 5 mL tube with cell strainer cap (Corning) and maintained at room temperature
491 protected from light for 15 minutes. Samples were acquired using FACS Canto System (BD
492 Biosciences, USA) and analyzed with ModFit LT software (Verity Software House).

493 **Protein extraction and Western Blot**

494 Cells were washed twice with ice-cold PBS, scraped and lysed on Lysis Buffer [20 mM Tris-HCl
495 pH 8, 10 mM EDTA, 150 mM NaCl, 1% Triton-X100] supplemented with protease inhibitor cocktail
496 (1:100 Sigma-Aldrich) and phosphatase inhibitors cocktail 2 and 3 (1:100 Sigma-Aldrich). Cell
497 lysates were centrifuged at 13000 rpm for 10 minutes at 4°C. Protein concentration was analyzed
498 using Pierce BCA Protein Assay kit (ThermoFisher Scientific) following manufacturer's
499 instructions. Equal amounts of protein lysates were resuspended in Laemmli SDS-sample buffer
500 and incubated at 95°C for 5 minutes. Proteins were separated on SDS-PAGE and transferred to
501 PVDF membranes (Millipore). Membranes were blocked with 5% non-fat dry milk (BioRad) in
502 Tris-buffered saline containing 0.1% Tween-20 (TBS-T) for 1 hour at room temperature.
503 Incubation of primary antibodies was performed overnight at 4°C in 5% non-fat dry milk or 3.5%
504 BSA (Sigma-Aldrich). After three washes in TBS-T, membranes were incubated for 1 hour at room
505 temperature with secondary antibodies (1:5000) diluted in 5% non-fat milk. Upon incubation,
506 membranes were washed three times with TBS-T and protein detection was performed by using
507 enhanced chemiluminescence kit (GE Healthcare). Blots were scanned with iBright detection
508 system (Thermo Fisher). All the antibodies used in this study are reported with the corresponding
509 working concentrations in **Table 3**.

510 **Immunoprecipitation**

511 U2OS cells transfected with WAPL-GFP expression vector or GFP-empty vector as negative
512 control were washed twice with ice-cold PBS and cellular pellets were kept at -80°C before lysis.
513 Cellular pellet was lysed in ice-cold IP-RIPA buffer [100 mM Tris-HCl pH7.5, 300 mM KCl, 10 mM
514 MgCl₂, 2 mM EGTA, 20% Glycerol and 1.6 % NP40] supplemented with protease inhibitors (2X),
515 phosphatase inhibitors cocktails (1X), PMSF 1mM and DTT 1mM. After 5 minutes incubation on
516 ice, collected samples were mechanically lysed with cold syringe and centrifuged at 13,000 rpm
517 for 5 minutes at 4 °C. Soluble fraction was subjected to BCA Pierce protein quantification. 1,500

518 μg of protein per sample were separated for immunoprecipitation at $1 \mu\text{g}/\mu\text{l}$ concentration. For the
519 immunoprecipitation, $30 \mu\text{l}$ of GFP-Trap beads (ChromoTek) were added to each lysate and
520 incubated by rotation overnight at 4°C . Immunoprecipitates were washed three times with IP-
521 RIPA buffer. Immunoprecipitated proteins were denatured by the addition of 2X sample buffer
522 followed by boiling for 10 minutes, resolved by 4 %-20 % Criterion TGX Gel (BIO-RAD)
523 electrophoresis and analyzed by immunoblotting. $20 \mu\text{g}$ of the total lysate were loaded as input
524 to control.

525 **Immunofluorescence**

526 Cells were grown as monolayers on coverslips and subjected to the indicated conditions. Cells
527 were fixed with 4% paraformaldehyde for 10 minutes at room temperature. After 5 minutes
528 washing with PBS, cells were permeabilized using 0.1% Triton X-100 in PBS for 10 minutes at
529 room temperature. Next, cells were blocked with 1% BSA/0.01% Triton X-100 in PBS plus 10 mM
530 Glycine for 30 minutes at room temperature. Cells were incubated with primary antibodies for one
531 hour at room temperature or overnight at 4°C . Following a series of PBS washes, cells were
532 incubated with secondary antibodies for 45 minutes at room temperature. After two washes of 5
533 minutes with PBS, coverslips were mounted using Vectashield Mounting Solution containing DAPI
534 (Vector Laboratories). All the antibodies used in this study are reported with the corresponding
535 working concentrations in **Table 2**.

536 **Vesicle acidification and detection assays in live cells**

537 U2OS cells were seeded onto glass coverslips and subjected to the indicated conditions. Live
538 cells were washed once with PBS and Magic Red (Immunochemistry Technologies) and
539 Lysosensor (Invitrogen) were added to cover the cell layer following manufacturer's instructions.
540 Cells were incubated for 10 minutes at room temperature before image acquisition.

541 **Image acquisition and analysis**

542 For detailed analysis, image acquisition was performed in Leica spectral confocal microscope
543 TCS SP5 using a 63x N.A 1.4 objective and LAS AF software or Carl Zeiss LSM880 confocal
544 microscope and ZEN software. Fluorophores were excited with Argon 488, DPSS 561, Diode 640
545 and Diode 405 lasers. Image analysis was performed using FIJI Image J software (NIH USA).

546 For toroidal nucleus and mitotic errors quantification, images were acquired using Nikon
547 Epifluorescence microscope using a 40x dry objective. Image analysis was performed using Cell
548 counter plugin from FIJI Image J software (NIH USA). Pearson's correlation coefficient was
549 calculated based on confocal images using FIJI ImageJ plugin Intensity Correlation Analysis.
550 Mitotic lysosomes size and number was analyzed with FIJI ImageJ fixing particles size from 0.3
551 μm^2 to infinity. The distribution of mitotic lysosomes was calculated with FIJI ImageJ plugin Radial
552 Profile Angle as previously described⁷².

553 **3D reconstitution**

554 Stacks of images acquired at optimal settings with Carl Zeiss LSM880 confocal microscope were
555 processed with IMARIS Software (Bitplane) for 3D image reconstruction and to generate in silico
556 animations and images.

557 **Live-cell time-lapse videos**

558 For mitotic delay analysis, U2OS H2B-GFP cells were grown onto glass bottom 8-well slides
559 (IBIDI). After indicated treatments, medium was replaced by FluoroBright medium (Gibco) and
560 live-cell imaging was performed on the Leica spectral confocal microscope TCS SP5. Images
561 were taken every 6 minutes and 33 seconds for a total time of 24 hours using the 63x glycerol
562 objective.

563 For lysosome trafficking analysis, U2OS cells stably expressing LAMP1-RFP and H2B-GFP were
564 grown onto glass bottom 8-well slides (IBIDI). After indicated treatments, medium was replaced
565 by FluoroBrite medium (Gibco) and live-cell imaging was performed on Carl Zeiss LSM880
566 confocal microscope. Images were taken every 5 minutes for a total time of 24 hours using the
567 63x glycerol objective.

568 For toroidal nucleus and nuclear lamina reformation assays, U2OS cells stably expressing H2B-
569 GFP and mCherry-Lamin A/C were grown onto bottom-glass 8 chambers slides (IBIDI). After
570 addition of FluoroBrite with indicated treatments, mitotic cell division was analyzed on a Carl Zeiss
571 LSM880 confocal microscope. For toroidal nucleus formation, images were taken every 93
572 seconds for 16 hours using the 63x glycerol objective. For nuclear envelope reformation
573 experiment, images were taken every 5 minutes for 16 hours using the 63x glycerol objective.

574 **Transmission Electron Microscopy (TEM)**

575 U2OS cells with or without ConcaA (10 nM) treatment for 24 hours were fixed with Glutaraldehyde
576 2.5% in Sodium Cacodylate Trihydrate 0.1 M pH 7.2 for 2 hours at 4°C. After three washes with
577 Sodium Cacodylate Trihydrate 0.1 M of 15 minutes each, samples were incubated for 2 hours
578 with Osmium tetroxide 1% in Sodium Cacodylate Trihydrate 0.1 M at room temperature. Samples
579 were washed three times for 15 minutes with Sodium Cacodylate Trihydrate 0.1 M. Then, samples
580 were processed through dehydration with Ethanol 30% to 100% gradually. Samples were then
581 embedded into Resin EPOXY. After sample orientation, polymerization occurred at 60°C for 48
582 hours. Samples were cut using ultramicrotome EM UC6 Leica, first in semithin of 250 nm and
583 then ultrathin of 70 nm. Image acquisition was performed with TEM microscope JEOL JEM-1011.
584 Images were analyzed and processed with FIJI ImageJ software (NIH).

585 **Mass Spectrometry**

586 Three replicates of treated samples were processed for protein extraction in RIPA lysis buffer
587 [Tris-HCl pH8 50mM, NaCl 150mM, NP-40 1%, Sodium deoxycholate 0.5%, SDS 0.1%]. Protein
588 concentration was determined and 50 µg of each sample was digested using a FASP (Filter-Aided
589 Sample Preparation) approach. Briefly, proteins were reduced with dithiothreitol 10 mM (60
590 minutes, 32°C) and alkylated with iodoacetamide 20 mM (30 minutes at 25°C in the dark).
591 Samples were loaded onto an Amicon Ultra filter 10 KDa, 0.5 mL (Millipore) to remove interfering
592 agents with 2 rounds of centrifugations/washes with 100 mM ammonium bicarbonate buffer
593 (13,600 g; 25 minutes at room temperature). Digestion was carried out in two steps: first, samples
594 were digested (1:50 w sample/w enzyme) with Lys-C (Wako) in 6 M urea buffer for 3 hours at
595 35°C, second, the samples were diluted 10-fold with 100 mM ammonium bicarbonate buffer and
596 digested with modified porcine trypsin (Promega-Gold) (1:25 w sample/w enzyme) for 16 hours
597 at 37°C. The resulting peptide mixture was recovered by centrifuging the filter. Then, the filter was
598 washed twice with 300 µL of 50 mM ammonium bicarbonate and once with 200 µL of 20%
599 acetonitrile/50 mM ammonium bicarbonate (13,600g for 25 min at room temperature). All the
600 fractions were pooled, and the final peptide mixture was acidified with formic acid. Finally, the
601 final volume of the acidified peptide solution was reduced on a SpeedVac vacuum system
602 (Thermo Fisher Scientific), and the peptide solution was desalinated with a C18 spin column
603 (Thermo Fisher Scientific) following supplier's indications.

604 Samples were analyzed in a Proxeon 1,000 liquid chromatographer coupled to an Orbitrap Fusion
605 Lumos (Thermo Fisher Scientific) mass spectrometer. Samples were re-suspended in 0.5%
606 formic acid in water, and 2 µL (1 µg/ µL) were injected for LC-MSMS analysis. Peptides were
607 trapped on an NTCC-360/75-3-123 LC column and separated using a C18 reverse phase LC
608 column-Easy Spray (Thermo Fisher Scientific). The gradient used for the elution of the peptides

609 was 1% to 35% in 90 minutes followed by a gradient from 35% to 85% in 10 minutes with 250
610 nL/min flow rate. Eluted peptides were subjected to electrospray ionization in an emitter needle
611 (PicoTip™, New Objective, Scientific Instrument Services) with an applied voltage of 2,000 V.
612 Peptide masses (m/z 300-1,700) were analyzed in data-dependent mode where a full scan MS
613 was acquired on the Orbitrap with a resolution of 60,000 FWHM at 400 m/z. Up to the 10 most
614 abundant peptides (minimum intensity of 500 counts) were selected from each MS scan and then
615 fragmented using CID (collision-induced dissociation) in the linear ion trap using helium as
616 collision gas with 38% normalized collision energy. The scan time settings were full MS at 250
617 ms and MSn at 120 ms. Generated raw data files were collected with Thermo Xcalibur (v.2.2)
618 (Thermo Fisher Scientific). MaxQuant 1.6.1.0 Software (Department for Proteomics and Signal
619 Transduction, Max-Planck Institute for Biochemistry) was used to search the raw data obtained
620 in the MS analyses against a SwissProt/Uniprot human database with Andromeda Search engine
621 (1.5.6.0). A target and decoy database were used to assess the false discovery rate (FDR).
622 Trypsin was chosen as enzyme and a maximum of two misscleavages were allowed.
623 Carbamidomethylation (C) was set as a fixed modification, whereas oxidation (M) and acetylation
624 (N-terminal) were used as variable modifications. Searches were performed using a peptide
625 tolerance of 7 ppm and a product ion tolerance of 0.5 Da. Resulting data files were filtered for
626 FDR <1%. Statistical analysis was performed in Perseus 1.6.2.1 (Department for Proteomics and
627 Signal Transduction, Max-Planck Institute for Biochemistry).

628 **Statistical Analysis**

629 Data was analyzed by Excel or GraphPad Prism4 software. Results are presented as Mean ±
630 S.D., for the indicated n independent experiments. Experimental data sets were compared by: (i)
631 Two-sampled, two-tailed Student's t-test for two experimental conditions sharing normal
632 distribution and variance (ii) One-way ANOVA test for more than 2 conditions sharing normal

633 distribution and variance. Multiple comparisons corrected using Bonferroni test (iii) Kruskal-Wallis
634 test for more than 2 conditions and data without assuming normal distribution. Multiple
635 comparisons corrected using Dunn's test.

636 **ACKNOWLEDGEMENTS**

637 We thank Dr. George Thomas, Dr. Sara Kozma and the rest of the members of the laboratory of
638 Cancer Metabolism for scientific inputs and sharing reagents. We thank Dr. Neus Agell for
639 providing H2B-GFP stable U2OS cells, Dr. Antonio Zorzano for MEFs Atg5 parental and KO and
640 Dr. Cristina Muñoz for siRNAs siAtg5 and sip62. We are grateful to Dr. Juan S. Bonifacino for
641 sharing KIF5A-GFP plasmid and to Dr. Fangwei Wang for WAPL-GFP plasmid. We also thank
642 the technical facilities at CCITUB for FACS analysis and confocal microscopy. We are grateful to
643 Dr. Joffrey Pelletier, Dr. Thomas Neufeld and Dr. Terje Johansen for their constructive comments
644 on the manuscript. This study was supported by grants to AT from Ministerio de Economía,
645 Industria y Competitividad (SAF2017-85561-R), which is part of Agencia Estatal de Investigación
646 (Co-funded by European Regional Development Fund. ERDF, a way to build Europe), by joint
647 grants to the Laboratory of Cancer Metabolism from Instituto de Salud Carlos III-Red Temática
648 de Investigación Cooperativa en Cáncer (RD12/0036/0049), and from Generalitat de Catalunya-
649 Suport als *Grups de Recerca de Catalunya* (2017SGR1743). EA was supported by Ministerio de
650 Educación, Cultura y Deporte (FPU13/05400) and SAF2017-85561-R. C.D. was supported by
651 Mayo Clinic/NIH training grant 5-T32-CA217836-02 and NIH grant RO1-HL125353 (through Edward
652 Hinchcliffe). C.M. was supported by Juan de la Cierva fellowship (IJCI-2015-24716) from Ministerio
653 de Ciencia Innovación y Universidades and by European Union's Horizon 2020 research and
654 innovation program under the Marie Skłodowska-Curie grant agreement (M-Lysosomes, 799000).
655 The authors declare no competing financial interests. We thank CERCA Program/Generalitat de
656 Catalunya for institutional support to IDIBELL.

657 **DISCLOSURE STATEMENT**

658 No potential conflict of interest was reported by the authors.

659 **AUTHORS CONTRIBUTIONS**

660 E.A. and C.M. conceived, designed and performed the experiments. C.D. performed experiments
661 for detection of toroidal nuclei in glioma cells. E.A., C.M., S.A. and A.T. analyzed and discussed
662 the data. E.A. and C.M. wrote the manuscript. A.T. and C.M. coordinated the study. All authors
663 intellectually contributed and commented on the manuscript.

664 **REFERENCES**

- 665 1. McClelland SE. Role of chromosomal instability in cancer progression. *Endocr Relat Cancer* 2017;
666 24:T23–31.
- 667 2. Bakhoun SF, Cantley LC. The Multifaceted Role of Chromosomal Instability in Cancer and Its
668 Microenvironment. *Cell* 2018; 174:1347–60.
- 669 3. Thompson SL, Bakhoun SF, Compton DA. Mechanisms of chromosomal instability. *Curr Biol CB*
670 2010; 20:R285–295.
- 671 4. Araujo AR, Gelens L, Sheriff RSM, Santos SDM. Positive Feedback Keeps Duration of Mitosis
672 Temporally Insulated from Upstream Cell-Cycle Events. *Mol Cell* 2016; 64:362–75.
- 673 5. Sullivan M, Morgan DO. Finishing mitosis, one step at a time. *Nat Rev Mol Cell Biol* 2007; 8:894–
674 903.
- 675 6. Bloom J, Cross FR. Multiple levels of cyclin specificity in cell-cycle control. *Nat Rev Mol Cell Biol*
676 2007; 8:149–60.
- 677 7. Peters J-M. The anaphase promoting complex/cyclosome: a machine designed to destroy. *Nat Rev*
678 *Mol Cell Biol* 2006; 7:644–56.
- 679 8. Pines J. Cubism and the cell cycle: the many faces of the APC/C. *Nat Rev Mol Cell Biol* 2011;
680 12:427–38.
- 681 9. Jia R, Guardia CM, Pu J, Chen Y, Bonifacino JS. BORC coordinates encounter and fusion of
682 lysosomes with autophagosomes. *Autophagy* 2017; 13:1648–63.

- 683 10. Guardia CM, Farías GG, Jia R, Pu J, Bonifacino JS. BORC Functions Upstream of Kinesins 1 and 3 to
684 Coordinate Regional Movement of Lysosomes along Different Microtubule Tracks. *Cell Rep* 2016;
685 17:1950–61.
- 686 11. Pu J, Schindler C, Jia R, Jarnik M, Backlund P, Bonifacino JS. BORC, a multisubunit complex that
687 regulates lysosome positioning. *Dev Cell* 2015; 33:176–88.
- 688 12. Mancias JD, Kimmelman AC. Mechanisms of Selective Autophagy in Normal Physiology and Cancer.
689 *J Mol Biol* 2016; 428:1659–80.
- 690 13. Lamark T, Svenning S, Johansen T. Regulation of selective autophagy: the p62/SQSTM1 paradigm |
691 *Essays in Biochemistry* [Internet]. [cited 2019 Sep 18]; Available from:
692 <http://essays.biochemistry.org/content/61/6/609.full-text.pdf>
- 693 14. Albertson R, Riggs B, Sullivan W. Membrane traffic: a driving force in cytokinesis. *Trends Cell Biol*
694 2005; 15:92–101.
- 695 15. Boucrot E, Kirchhausen T. Endosomal recycling controls plasma membrane area during mitosis.
696 *Proc Natl Acad Sci* 2007; 104:7939–44.
- 697 16. Jongsma MLM, Berlin I, Neefjes J. On the move: organelle dynamics during mitosis. *Trends Cell Biol*
698 2015; 25:112–24.
- 699 17. Eskelinen E-L, Prescott AR, Cooper J, Brachmann SM, Wang L, Tang X, Backer JM, Lucocq JM.
700 Inhibition of autophagy in mitotic animal cells. *Traffic Cph Den* 2002; 3:878–93.
- 701 18. Furuya T, Kim M, Lipinski M, Li J, Kim D, Lu T, Shen Y, Rameh L, Yankner B, Tsai L-H, et al. Negative
702 regulation of Vps34 by Cdk mediated phosphorylation. *Mol Cell* 2010; 38:500–11.
- 703 19. Lu G, Yi J, Gubas A, Wang Y-T, Wu Y, Ren Y, Wu M, Shi Y, Ouyang C, Tan HWS, et al. Suppression of
704 autophagy during mitosis via CUL4-RING ubiquitin ligases-mediated WIP1 polyubiquitination and
705 proteasomal degradation. *Autophagy* 2019; :1–18.
- 706 20. Loukil A, Zonca M, Rebouissou C, Baldin V, Coux O, Biard-Piechaczyk M, Blanchard J-M, Peter M.
707 High-resolution live-cell imaging reveals novel cyclin A2 degradation foci involving autophagy. *J Cell*
708 *Sci* 2014; 127:2145–50.
- 709 21. Li Z, Zhang X. Autophagy in mitotic animal cells. *Sci Bull* 2016; 61:105–7.
- 710 22. Liu L, Xie R, Nguyen S, Ye M, McKeehan WL. Robust autophagy/mitophagy persists during mitosis.
711 *Cell Cycle Georget Tex* 2009; 8:1616–20.
- 712 23. Yuan F, Jin X, Li D, Song Y, Zhang N, Yang X, Wang L, Zhu W-G, Tian C, Zhao Y. ULK1 phosphorylates
713 Mad1 to regulate spindle assembly checkpoint. *Nucleic Acids Res* 2019;
- 714 24. Holdgaard SG, Cianfanelli V, Pupo E, Lambrughli M, Lubas M, Nielsen JC, Eibes S, Maiani E, Harder
715 LM, Wesch N, et al. Selective autophagy maintains centrosome integrity and accurate mitosis by
716 turnover of centriolar satellites. *Nat Commun* 2019; 10:4176.

- 717 25. Joachim J, Razi M, Judith D, Wirth M, Calamita E, Encheva V, Dynlacht BD, Snijders AP, O'Reilly N,
718 Jefferies HBJ, et al. Centriolar Satellites Control GABARAP Ubiquitination and GABARAP-Mediated
719 Autophagy. *Curr Biol* 2017; 27:2123-2136.e7.
- 720 26. Mathew R, Kongara S, Beaudoin B, Karp CM, Bray K, Degenhardt K, Chen G, Jin S, White E.
721 Autophagy suppresses tumor progression by limiting chromosomal instability. *Genes Dev* 2007;
722 21:1367-81.
- 723 27. Rieder CL, Maiato H. Stuck in Division or Passing through: What Happens When Cells Cannot
724 Satisfy the Spindle Assembly Checkpoint. *Dev Cell* 2004; 7:637-51.
- 725 28. Abella N, Brun S, Calvo M, Tapia O, Weber JD, Berciano MT, Lafarga M, Bachs O, Agell N. Nucleolar
726 Disruption Ensures Nuclear Accumulation of p21 upon DNA Damage. *Traffic* 2010; 11:743-55.
- 727 29. Verstraeten VLRM, Peckham LA, Olive M, Capell BC, Collins FS, Nabel EG, Young SG, Fong LG,
728 Lammerding J. Protein farnesylation inhibitors cause donut-shaped cell nuclei attributable to a
729 centrosome separation defect. *Proc Natl Acad Sci U S A* 2011; 108:4997-5002.
- 730 30. Liu Y, Zhang Z, Liang H, Zhao X, Liang L, Wang G, Yang J, Jin Y, McNutt MA, Yin Y. Protein
731 Phosphatase 2A (PP2A) Regulates EG5 to Control Mitotic Progression. *Sci Rep [Internet]* 2017
732 [cited 2019 Mar 8]; 7. Available from: <http://www.nature.com/articles/s41598-017-01915-w>
- 733 31. Ishikawa K, Kamohara Y, Tanaka F, Haraguchi N, Mimori K, Inoue H, Mori M. Mitotic centromere-
734 associated kinesin is a novel marker for prognosis and lymph node metastasis in colorectal cancer.
735 *Br J Cancer* 2008; 98:1824-9.
- 736 32. Yao X, Abrieu A, Zheng Y, Sullivan KF, Cleveland DW. CENP-E forms a link between attachment of
737 spindle microtubules to kinetochores and the mitotic checkpoint. *Nat Cell Biol* 2000; 2:484-91.
- 738 33. Hashizume R, Smirnov I, Liu S, Phillips JJ, Hyer J, McKnight TR, Wendland M, Prados M, Banerjee A,
739 Nicolaidis T, et al. Characterization of a diffuse intrinsic pontine glioma cell line: implications for
740 future investigations and treatment. *J Neurooncol* 2012; 110:305-13.
- 741 34. Nagaraja S, Vitanza NA, Woo P, Taylor KR, Liu F, Zhang L, Li M, Meng W, Ponnuswami A, Sun W, et
742 al. Transcriptional Dependencies in Diffuse Intrinsic Pontine Glioma. *Cancer Cell* 2017; 31:635-
743 652.e6.
- 744 35. Zhang L, Peterson TE, Lu VM, Parney IF, Daniels DJ. Antitumor activity of novel pyrazole-based
745 small molecular inhibitors of the STAT3 pathway in patient derived high grade glioma cells. *PLoS*
746 *ONE [Internet]* 2019 [cited 2019 Sep 23]; 14. Available from:
747 <https://www.ncbi.nlm.nih.gov/pmc/articles/PMC6667205/>
- 748 36. Chan K-M, Fang D, Gan H, Hashizume R, Yu C, Schroeder M, Gupta N, Mueller S, James CD, Jenkins
749 R, et al. The histone H3.3K27M mutation in pediatric glioma reprograms H3K27 methylation and
750 gene expression. *Genes Dev* 2013; 27:985-90.
- 751 37. Mueller S, Hashizume R, Yang X, Kolkowitz I, Olow AK, Phillips J, Smirnov I, Tom MW, Prados MD,
752 James CD, et al. Targeting Wee1 for the treatment of pediatric high-grade gliomas. *Neuro-Oncol*
753 2014; 16:352-60.

- 754 38. Mauvezin C, Nagy P, Juhász G, Neufeld TP. Autophagosome–lysosome fusion is independent of V-
755 ATPase-mediated acidification. *Nat Commun* 2015; 6:7007.
- 756 39. Kim OH, Lim JH, Woo KJ, Kim Y-H, Jin I-N, Han ST, Park J-W, Kwon TK. Influence of p53 and
757 p21Waf1 expression on G2/M phase arrest of colorectal carcinoma HCT116 cells to proteasome
758 inhibitors. *Int J Oncol* 2004; 24:935–41.
- 759 40. Huszar D, Theoclitou M-E, Skolnik J, Herbst R. Kinesin motor proteins as targets for cancer therapy.
760 *Cancer Metastasis Rev* 2009; 28:197–208.
- 761 41. Pontén J, Saksela E. Two established in vitro cell lines from human mesenchymal tumours. *Int J*
762 *Cancer* 1967; 2:434–47.
- 763 42. Fabregat A, Jupe S, Matthews L, Sidiropoulos K, Gillespie M, Garapati P, Haw R, Jassal B, Korninger
764 F, May B, et al. The Reactome Pathway Knowledgebase. *Nucleic Acids Res* 2018; 46:D649–55.
- 765 43. Stein LD. Using the Reactome Database. *Curr Protoc Bioinforma* 2004; 7:8.7.1-8.7.16.
- 766 44. Shintomi K, Hirano T. Releasing cohesin from chromosome arms in early mitosis: opposing actions
767 of Wapl-Pds5 and Sgo1. *Genes Dev* 2009; 23:2224–36.
- 768 45. Pohl C, Jentsch S. Midbody ring disposal by autophagy is a post-abscission event of cytokinesis. *Nat*
769 *Cell Biol* 2009; 11:65–70.
- 770 46. Akutsu M, Dikic I, Bremm A. Ubiquitin chain diversity at a glance. *J Cell Sci* 2016; 129:875–80.
- 771 47. Rogov V, Dötsch V, Johansen T, Kirkin V. Interactions between Autophagy Receptors and Ubiquitin-
772 like Proteins Form the Molecular Basis for Selective Autophagy. *Mol Cell* 2014; 53:167–78.
- 773 48. Hewitt G, Carroll B, Sarallah R, Correia-Melo C, Ogrodnik M, Nelson G, Otten EG, Manni D,
774 Antrobus R, Morgan BA, et al. SQSTM1/p62 mediates crosstalk between autophagy and the UPS in
775 DNA repair. *Autophagy* 2016; 12:1917–30.
- 776 49. Nam T, Han JH, Devkota S, Lee H-W. Emerging Paradigm of Crosstalk between Autophagy and the
777 Ubiquitin-Proteasome System. *Mol Cells* 2017; 40:897–905.
- 778 50. Peters J-M, Nishiyama T. Sister Chromatid Cohesion. *Cold Spring Harb Perspect Biol* 2012;
779 4:a011130.
- 780 51. Hassler M, Shaltiel IA, Haering CH. Towards a Unified Model of SMC Complex Function. *Curr Biol*
781 2018; 28:R1266–81.
- 782 52. Haarhuis JHI, Elbatsh AMO, van den Broek B, Camps D, Erkan H, Jalink K, Medema RH, Rowland BD.
783 WAPL-mediated removal of cohesin protects against segregation errors and aneuploidy. *Curr Biol*
784 *CB* 2013; 23:2071–7.
- 785 53. Losada A, Hirano M, Hirano T. Cohesin release is required for sister chromatid resolution, but not
786 for condensin-mediated compaction, at the onset of mitosis. *Genes Dev* 2002; 16:3004–16.

- 787 54. Hara K, Zheng G, Qu Q, Liu H, Ouyang Z, Chen Z, Tomchick DR, Yu H. Structure of cohesin
788 subcomplex pinpoints direct shugoshin–Wapl antagonism in centromeric cohesion. *Nat Struct Mol*
789 *Biol* 2014; 21:864–70.
- 790 55. Nishiyama T, Ladurner R, Schmitz J, Kreidl E, Schleiffer A, Bhaskara V, Bando M, Shirahige K, Hyman
791 AA, Mechtler K, et al. Sororin Mediates Sister Chromatid Cohesion by Antagonizing Wapl. *Cell*
792 2010; 143:737–49.
- 793 56. Nakajima M, Kumada K, Hatakeyama K, Noda T, Peters J-M, Hirota T. The complete removal of
794 cohesin from chromosome arms depends on separase. *J Cell Sci* 2007; 120:4188–96.
- 795 57. Misulovin Z, Pherson M, Gause M, Dorsett D. Brca2, Pds5 and Wapl differentially control cohesin
796 chromosome association and function. *PLoS Genet* 2018; 14:e1007225.
- 797 58. Oikawa K, Ohbayashi T, Kiyono T, Nishi H, Isaka K, Umezawa A, Kuroda M, Mukai K. Expression of a
798 novel human gene, human wings apart-like (hWAPL), is associated with cervical carcinogenesis and
799 tumor progression. *Cancer Res* 2004; 64:3545–9.
- 800 59. Losada A. Functional contribution of Pds5 to cohesin-mediated cohesion in human cells and
801 *Xenopus* egg extracts. *J Cell Sci* 2005; 118:2133–41.
- 802 60. Ohbayashi T, Oikawa K, Yamada K, Nishida-Umehara C, Matsuda Y, Satoh H, Mukai H, Mukai K,
803 Kuroda M. Unscheduled overexpression of human WAPL promotes chromosomal instability.
804 *Biochem Biophys Res Commun* 2007; 356:699–704.
- 805 61. Chude CI, Amaravadi RK. Targeting Autophagy in Cancer: Update on Clinical Trials and Novel
806 Inhibitors. *Int J Mol Sci* [Internet] 2017 [cited 2018 Sep 16]; 18. Available from:
807 <https://www.ncbi.nlm.nih.gov/pmc/articles/PMC5486101/>
- 808 62. Jiang P, Mizushima N. Autophagy and human diseases. *Cell Res* 2014; 24:69–79.
- 809 63. Simonetti G, Bruno S, Padella A, Tenti E, Martinelli G. Aneuploidy: Cancer strength or vulnerability?
810 *Int J Cancer* 2018;
- 811 64. Vessoni AT, Filippi-Chiela EC, Menck CF, Lenz G. Autophagy and genomic integrity. *Cell Death Differ*
812 2013; 20:1444–54.
- 813 65. White E, DiPaola RS. The Double-edged Sword of Autophagy Modulation in Cancer. *Clin Cancer Res*
814 *Off J Am Assoc Cancer Res* 2009; 15:5308–16.
- 815 66. Crasta K, Ganem NJ, Dagher R, Lantermann AB, Ivanova EV, Pan Y, Nezi L, Protopopov A,
816 Chowdhury D, Pellman D. DNA breaks and chromosome pulverization from errors in mitosis.
817 *Nature* 2012; 482:53–8.
- 818 67. Rello-Varona S, Lissa D, Shen S, Niso-Santano M, Senovilla L, Mariño G, Vitale I, Jemaá M, Harper F,
819 Pierron G, et al. Autophagic removal of micronuclei. *Cell Cycle Georget Tex* 2012; 11:170–6.

- 820 68. Bartsch K, Knittler K, Borowski C, Rudnik S, Damme M, Aden K, Spehlmann ME, Frey N, Saftig P,
821 Chalaris A, et al. Absence of RNase H2 triggers generation of immunogenic micronuclei removed by
822 autophagy. *Hum Mol Genet* 2017; 26:3960–72.
- 823 69. Hatch EM, Fischer AH, Deerinck TJ, Hetzer MW. Catastrophic Nuclear Envelope Collapse in Cancer
824 Cell Micronuclei. *Cell* 2013; 154:47–60.
- 825 70. Hintzsche H, Hemmann U, Poth A, Utesch D, Lott J, Stopper H. Fate of micronuclei and
826 micronucleated cells. *Mutat Res Mutat Res* 2017; 771:85–98.
- 827 71. Klionsky DJ, Abdelmohsen K, Abe A, Abedin MJ, Abeliovich H, Acevedo Arozena A, Adachi H, Adams
828 CM, Adams PD, Adeli K, et al. Guidelines for the use and interpretation of assays for monitoring
829 autophagy (3rd edition). *Autophagy* 2016; 12:1–222.
- 830 72. Chung JY-M, Steen JA, Schwarz TL. Phosphorylation-Induced Motor Shedding is Required at Mitosis
831 for Proper Distribution and Passive Inheritance of Mitochondria. *Cell Rep* 2016; 16:2142–55.

832 **FIGURE LEGENDS**

833 **Figure 1. Autophagic flux and lysosome-dependent degradation are active in dividing cells.**

834 **(A)** Representative single focal plan (1Z) confocal images of U2OS cells undergoing mitosis
835 labelled with lysosomal marker LAMP2 (green). Interphase cell and distinct mitotic subphases are
836 detectable with DNA staining with DAPI (blue). Scale bar, 10 μm . **(B)** Quantification of lysosome
837 number per cell in interphase compared to each mitotic subphases. Error bars represent S.D. of
838 ≥ 10 images. **(C)** Quantification of lysosome average size per cell in interphase and for each
839 mitotic subphases. Error bars represent S.D. of ≥ 10 images. **(D)** Upper panel: Analysis of the
840 distribution of lysosomes (green) and DNA (blue) in interphase and for each mitotic subphases
841 using Radial Profile Angle ImageJ plugin. A Radius of 20 μm was maintained constant for the
842 analysis. Lower panel: representative image of a cell in each analyzed phase. **(E)** Representative
843 single focal plan confocal images of U2OS H2B-GFP stable cells in interphase or undergoing
844 mitosis were stained with LysoTracker (green – arbitrary color) for lysosomes detection, Magic
845 Red (red) for active cathepsin B, H2B-GFP (blue – arbitrary color) for DNA staining. Scale bar, 10
846 μm . **(F)** Schematic representation of the synchronization protocol established for U2OS cells. **(G)**
847 Cell cycle analysis of cells at T0 (before release of the reversible CDK1 inhibitor – RO3306) and

848 of cells after release from RO3306 incubated either with normal growing media (CTRL) or with 10
849 nM ConCA-containing growing media. Percentage of cells in G1, S and G2/M cell cycle phases
850 are represented under the experimental conditions. **(H)** Analysis of autophagic flux by Western
851 Blot detection with specific antibodies of autophagic proteins p62 and LC3 in cell fractions of panel
852 G synchronized as in panel F. β -actin protein level was used as loading control. **(I)** Representative
853 maximal projection ($z \geq 15$) of confocal images of U2OS cells in interphase or cells undergoing
854 mitosis. Endogenous autophagic proteins LC3 (red) and p62 (green) were detected by
855 immunofluorescence and DNA was marked with DAPI (blue). Pearson's correlation coefficient (r)
856 was calculated for each analyzed condition ($n \geq 10$). Scale bar, 10 μm . **(J)** TEM images show
857 mitotic cells undergoing mitotic exit. Arrowheads indicate autophagic vesicles and lysosomes and
858 yellow asterisks point out mitochondria. Scale bars, as indicated. **Panels B and C**, statistical
859 significance between interphase and mitotic subphases is represented as: * $p < 0.05$, ** $p < 0.005$,
860 *** $p < 0.001$

861 **Figure 2. Lysosome impairment delays mitotic progression and leads to mitotic errors and**
862 **an atypical nuclear phenotype. (A-B)** U2OS cells were either treated with ConCA 10 nM for 24
863 hours **(A)** or transiently transfected with silencing RNA against KIF5B (siKIF5B) **(B)**. Single plan
864 confocal images show LAMP2-positive lysosomes (green) detected by immunofluorescence in
865 cells undergoing mitosis. DNA is labelled with DAPI (blue). Scale bar, 10 μm . **(C-D)** Comparison
866 of the number of lysosomes per cell **(C)** or the average lysosome size **(D)** in interphase and each
867 mitotic subphases in control, ConCA-treated or KIF5B-depleted cells. Line represents the mean
868 in each condition. Total images analyzed ≥ 10 per condition. **(E)** Intracellular distribution of
869 lysosomes in interphase and in each mitotic subphases in control and KIF5B-depleted cells. Total
870 images analyzed ≥ 10 per condition. **(F)** H2B-GFP U2OS cells were subjected to time-lapse
871 imaging for 24 hours every 6 minutes 33 seconds. Single focal plan of representative images of
872 control cells, cells treated with ConCA 10 nM or depleted for KIF5B (siKIF5B) for 48 hours

873 undergoing mitosis are shown. H2B-GFP is depicted in grayscale (arbitrary color). Scale bars, 5
874 μm . **(G)** Quantification of mitotic timing of the indicated experimental conditions was performed
875 from prophase (chromosomes condensation) to telophase (chromosomes decondensation). Error
876 bars represent 5-95 percentiles of mitosis ≥ 90 . **(H)** Representative images of misaligned
877 metaphase plate and chromosome bridges. Scale bar, 5 μm . **(I-J)** U2OS cells were synchronized
878 at late G2 phase and released with or without Conca for 1 hour **(I)** or 3 hours **(J)**. DAPI staining
879 was used for DNA detection. Chromosome misalignment **(I)** and chromosomal bridges **(J)** were
880 quantified compared to total number of metaphases and anaphases, respectively. Error bars
881 represent S.D. of $n=3$ independent experiments (>200 cells). **(K-L)** U2OS cells depleted for KIF5B
882 (siKIF5B) or transfected with siRNA control (siNT) were synchronized and released for 1 hour **(K)**
883 or 3 hours **(L)** to determine the percentage of chromosome misalignment or chromosome bridges
884 relative to the total number of cells undergoing metaphase or anaphase, respectively. Error bars
885 represent S.D. of $n=3$ experiments (>150 cells). In **Panels G** and **I-L**, statistical significance is
886 represented as: * $p < 0.05$, ** $p < 0.005$, *** $p < 0.001$.

887 **Figure 3. Toroidal nucleus is a novel biomarker for chromosomal instability in interphase**
888 **cells.** **(A)** Representative image of toroidal nucleus. U2OS cells were fixed and stained with DAPI
889 for DNA detection. Scale bar, 5 μm . **(B)** Live imaging of H2B-GFP U2OS cells undergoing cell
890 cycle for 16 hours every 93 seconds. Mosaic of single focal plan images indicate aberrant nucleus
891 formation upon cell division. Scale bar, 10 μm . **(C-E)** U2OS cells were fixed and
892 immunofluorescence was performed using nucleolin antibody for nucleolus detection **(C)**, Lamin
893 B1 antibody for nuclear envelope staining **(D)** or LAMP2 antibody to mark lysosomes **(E)** and
894 DAPI for DNA labelling. Scale bar, 5 μm . **(F)** 3D reconstruction using IMARIS software was
895 performed from confocal images stack of toroidal nucleus (z every 0.1 μm for 11 μm). Blue
896 corresponds to DAPI-stained nucleus and yellow dots mark LAMP2-positive lysosomes. **(G)**
897 U2OS cells were treated with Conca for 24 hours, fixed and prepared for TEM. Images show

898 toroidal nucleus surrounded by the nuclear envelope. Abbreviations used: NE: nuclear envelop,
899 N: nucleus, Cyt: cytosol, AV: autophagic vesicles. Scale bars, as indicated. **(H)** Analysis of live
900 imaging experiment by following cell division of H2B-GFP U2OS cells for 24 hours every 9
901 minutes. Mitotic cells were detected and visualized to quantify the number of those with detectable
902 mitotic errors (misaligned chromosomes or chromosomal bridges) and those generating toroidal
903 nucleus. Linear regression was analyzed and the corresponding Pearson coefficient (r) was
904 calculated. **(I)** Analysis of the percentage of toroidal nucleus formed upon non-apparent mitotic
905 error or as a consequence of mitotic errors. Error bars represent S.D. of 295 mitosis. **(J)** U2OS
906 cells were depleted for KIF11 or MCAK for 48 hours using silencing RNA or treated with Monastrol
907 100 μ M or Nocodazole 1 μ M for 24 hours. Quantification of toroidal nuclei formed under these
908 conditions was performed by detection of DAPI-stained nuclei. Error bars represent S.D. of $n > 3$
909 experiments (10 fields / experiment). **(K)** Table summarizing a screen for toroidal nuclei through
910 various cell lines. Fold-increase was calculated upon ConcA treatment (10 nm for 24 h). **(L)**
911 Representative images of toroidal nuclei in screened cell lines from panel K. Panels **I** and **J**
912 statistical significance is represented as: * $p < 0.05$, ** $p < 0.005$, *** $p < 0.001$.

913 **Figure 4. Toroidal nucleus frequency increases upon impairment of lysosome trafficking**
914 **and acidification capacity.** **(A)** U2OS cells were treated with ConcA (10 nM) for 24 hours or
915 depleted for KIF5B for 48 hours using silencing RNA. Error bars represent S.D. of $n > 5$
916 experiments. **(B)** Representative confocal single plans showing morphology and distribution of
917 endogenous lysosomes (LAMP2 in green) under experimental conditions of panel A. Nuclei were
918 labelled with DAPI in blue. Scale bar, 10 μ m. **(C)** U2OS cells were treated with Chloroquine CQ
919 (10 μ M) or depleted for the V0c subunit of the v-ATPase (siATP6V0c) for 48 hours. Error bars
920 represent S.D. of $n > 3$ experiments. **(D)** Representative single plan confocal images of U2OS
921 cells treated as in panel **C**. Lysosomes were detected with LAMP2 antibody and nuclei were
922 stained with DAPI. Scale bar, 10 μ m. **(E)** U2OS cells were depleted for BORC-associated proteins

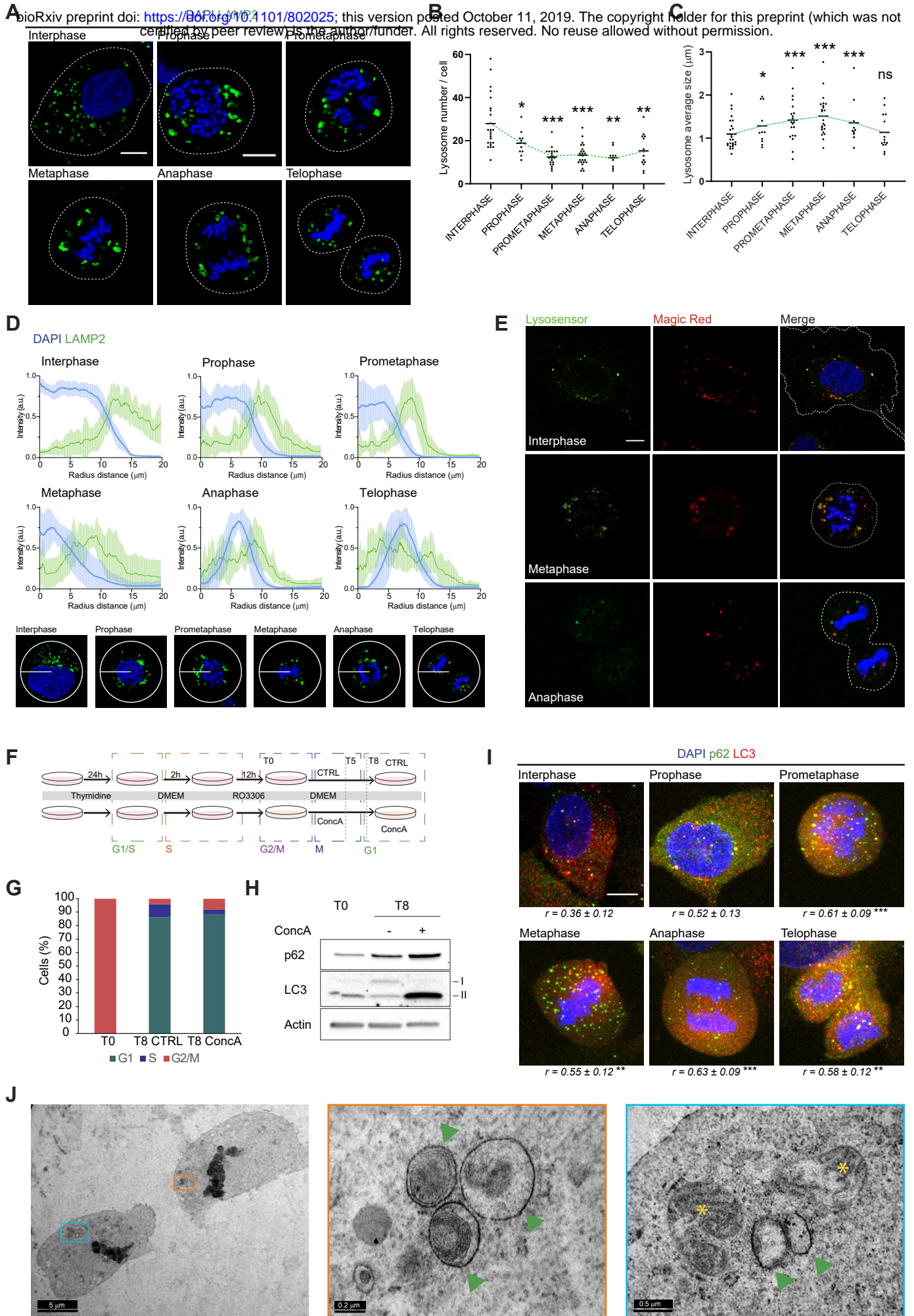
923 SKIP or Arl8b using silencing RNA for 48 hours. Error bars represent S.D. of $n > 3$ experiments.
924 **(F)** Representative images of LAMP2-positive lysosomes (green) under the indicated conditions
925 (panel E). Nuclei are stained with DAPI (blue). Scale bar, 10 μm . **(G)** U2OS cells were transfected
926 with KIF5B silencing RNA and/or with KIF5A-GFP overexpression plasmid. Error bars represent
927 S.D. of $n > 3$ experiments. **(H)** U2OS cells were depleted for KIF5B or SKIP and the next day
928 treated or not with ConcA for 24 hours. Error bars represent S.D. of $n > 3$ experiments. In panels
929 **A, C, E** and **G-H** nuclei were stained with DAPI for detection of toroidal nuclei compared to total
930 number of cells. Statistical significance is represented as: * $p < 0.05$, ** $p < 0.005$, *** $p < 0.001$,
931 ns: $p > 0.05$.

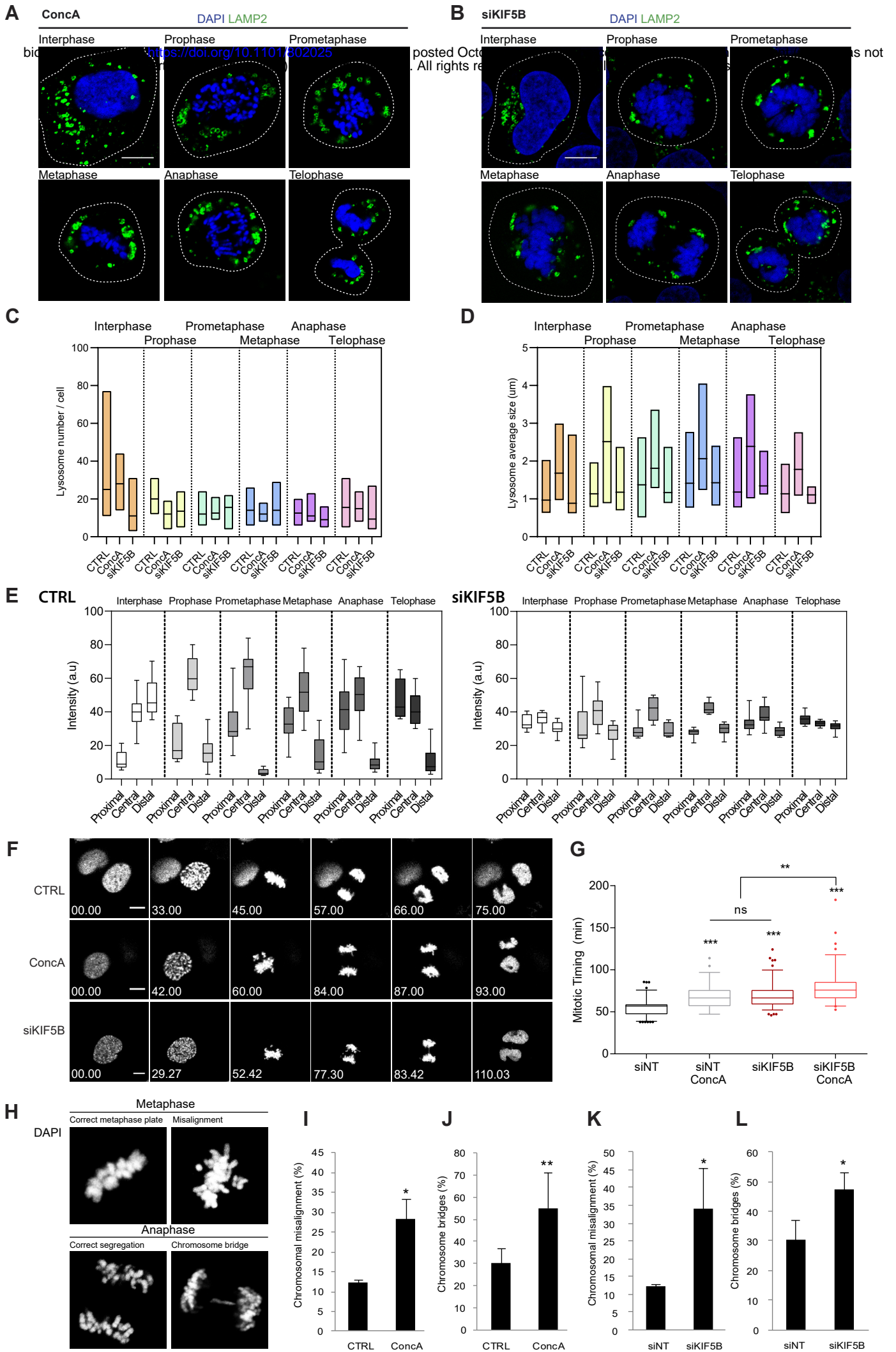
932 **Figure 5. Alterations of macroautophagy increase mitotic errors and toroidal nucleus**
933 **formation.** **(A)** U2OS cells were depleted for Atg5 for 48 hours and treated or not with ConcA for
934 24 hours. Error bars represent S.D. of $n > 3$ experiments. **(B-C)** Quantification of mitotic errors
935 (chromosome misalignment and chromosome bridges, respectively) in U2OS cells control (siNT)
936 or depleted for Atg5 (siAtg5) for 48 hours under normal growing condition (CTRL) or treated with
937 ConcA (10 nM for 24 h). Error bars represent S.D. of $n=4$ experiments (>300 cells). **(D)** Validation
938 of Atg5 depletion and ConcA efficacy in MEFs Atg5 $+/+$ and $-/-$ by Western Blot. β -actin was used
939 as loading control. **(E)** MEF Atg5 $+/+$ and Atg5 $-/-$ were subjected or not to ConcA treatment for
940 24 hours. DNA was labelled with DAPI and frequency of toroidal nuclei was quantified. Error bars
941 represent S.D. of $n=3$ experiments. **(F)** Representative image of toroidal nucleus in MEF Atg5 KO
942 cells. Scale bar, 5 μm . **(G-H)** Quantification of mitotic errors (chromosome misalignment and
943 chromosome bridges, respectively) in MEF Atg5 $+/+$ and Atg5 $-/-$. Error bars represent S.D. of
944 $n=5$ experiments (>100 cells). Panels **A-C, E** and **G-H**, * represents the statistical significance of
945 ConcA inhibitory effect compared to control, while # represents the effects of Atg5 genetic
946 depletion. * $p < 0.05$, ** $p < 0.005$, *** $p < 0.001$, ns: $p > 0.05$, # $p < 0.05$ and ## $p < 0.005$.

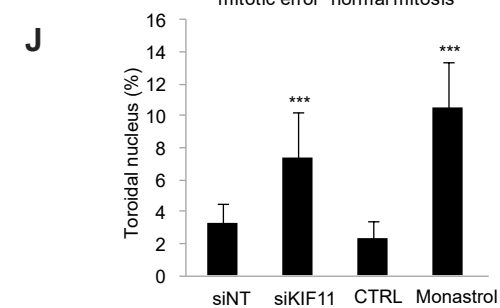
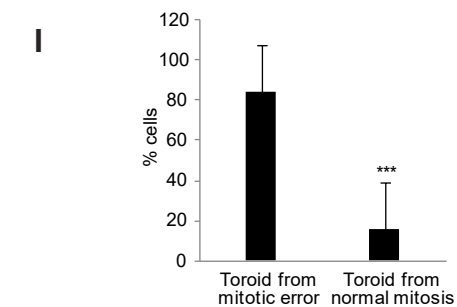
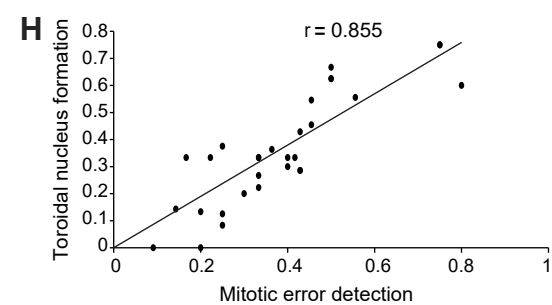
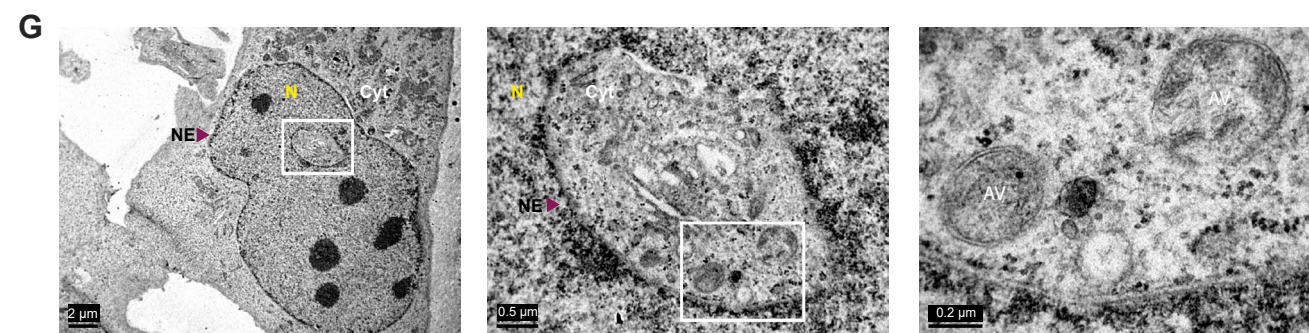
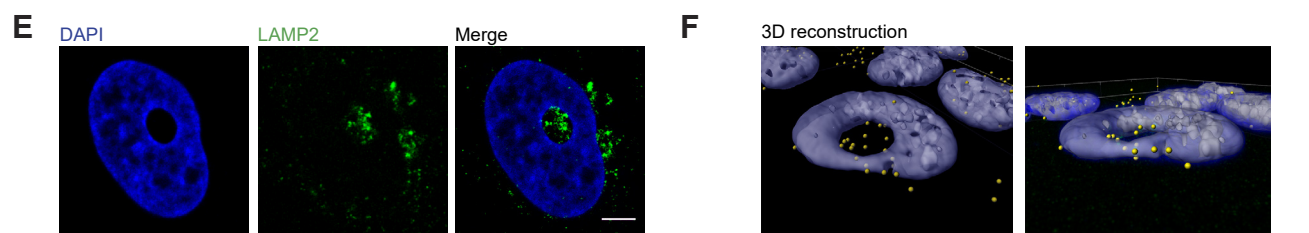
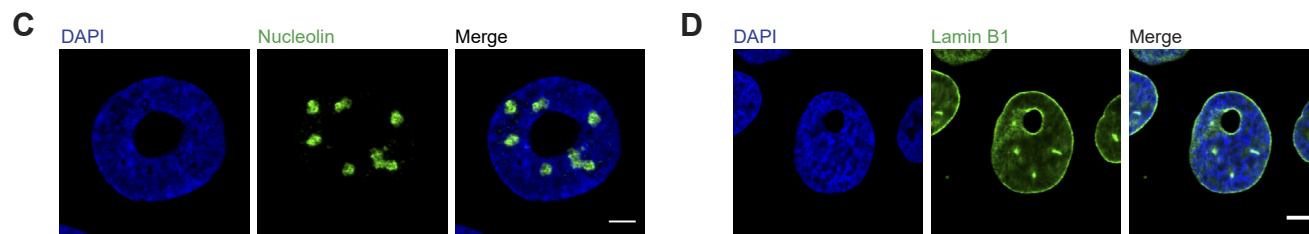
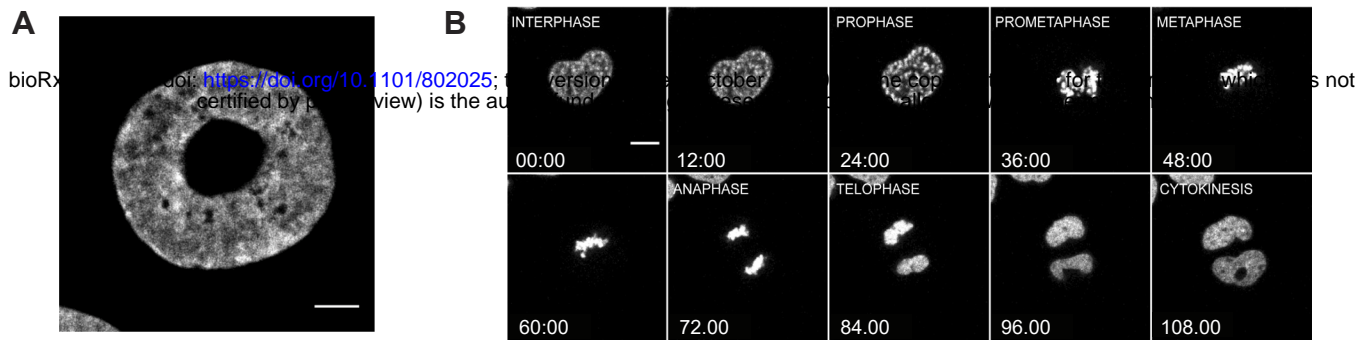
947 **Figure 6. Identification of novel mitotic lysosomal substrates.** (A) Venn diagram representing
948 proteins detected by mass spectrometry of synchronized U2OS cells released in growing media
949 (CTRL) or ConcA-containing media. (B) Volcano plot depicting significant fold changes (FC) (\log_2)
950 in protein abundances in cells treated with 10 nM ConcA. Three independent experiments were
951 analyzed per condition. Dots denote the 1749 unique proteins detected in pre-filtered samples.
952 Threshold at q -value < 0.05 depicts peptides significantly modified under experimental conditions.
953 Blue dots represent peptides with $FC < 0.8$. Orange dots correspond to peptides presenting a FC
954 > 1.2 . Within these candidates, red dots indicate target proteins WAPL, p62 and PDS5B. (C)
955 Table summarizing the 20 candidates identified by mass spectrometry that are clustered in the
956 Gene Ontology (GO) group GO:1903047 of mitotic cell cycle progress. (D) Western Blot of
957 synchronized U2OS mitotic cell fractions after mitotic cell enrichment by shake-off. Protein levels
958 of WAPL, PDS5B, p62 and LC3 were detected. β actin was used as loading control. (E)
959 Quantification of WAPL, PDS5B, p62 and LC3-II protein levels in experimental conditions as in
960 panel D and normalized to β actin protein level. Error bars represent S.D. of $n=3$ experiments. (F)
961 MEFs Atg5 $+/+$ and $-/-$ under normal growing conditions were subjected to shake-Off. Mitotic
962 enriched cell fractions were then analyzed by Western-Blot and accumulation of WAPL and
963 PDS5B was detected in MEF Atg5 $-/-$. β -actin was used as loading control. (G) Quantification of
964 WAPL and PDS5B protein levels from panel F normalized to β -actin loading control. Error bars
965 represent S.D. of $n=3$ experiments. (H) Immunoprecipitation of exogenous WAPL-GFP in U2OS
966 cells treated or not with 10 nM ConcA for 24 hours. Direct interaction between WAPL and p62
967 was detected by Western-Blot. Cells expressing exogenous GFP tag were used as negative
968 control. Statistical significance is represented as: * $p < 0.05$, ** $p < 0.005$, *** $p < 0.001$, ns: $p >$
969 0.05.

970 **Figure 7. Impairment of lysosomes in mitotic cells leads to chromosomal instability.**
971 Lysosomal function is required for the maintenance of correct cell division and faithful

972 transmission of genetic material in the two daughter cells. Functional lysosomes degrade
973 essential mitotic factors necessary for appropriate chromosome segregation. On the contrary,
974 when lysosomes are dysfunctional either by impairment of their trafficking or acidification capacity,
975 mitotic cells are prompt to accumulate mitotic errors, to generate toroidal nucleus and mitosis is
976 delayed. These alterations are key features of chromosomal instability.







K

Source	Cell Type	Name	Toroidal Nuclei	Fold-increase upon ConcA
Human	Osteosarcoma	U2OS	YES	3.16
Human	Cervix epitheloid carcinoma	HeLa	YES	3.57
Human	Lung carcinoma	A549	YES	8.38
Human	Colorectal carcinoma	HCT116	NO	
Human	Hepato cellular carcinoma	HuH7	NO	
Human	Breast adenocarcinoma	MCF7	NO	
Human	Colon carcinoma	RKO	NO	
Human	Colorectal adenocarcinoma	LOVO	NO	
Human	Pediatric high-grade glioma	MC-PED17	NO	
Human	Pediatric diffuse intrinsic pontine glioma	SF-7761	YES	2.32
Human	Pediatric diffuse intrinsic pontine glioma	SF-8628	YES	ND
Human	Pediatric diffuse intrinsic pontine glioma	SU-DIPG-XVII	YES	1.52
Human	Skin fibroblast	HFF-1	YES	2.19
Human	Normal Kidney epithelium	HEK293-T	NO	
Mouse	Embryonic fibroblasts	MEF	YES	5.11

